CHARACTERIZATION AND APPLICATION OF A LENS SYSTEM DESIGN FOR ENGINE DIAGNOSTICS AND 3D RECONSTRUCTIONS

by

Vaishnavi Radkar

A Thesis

Submitted to the Faculty of Purdue University

In Partial Fulfillment of the Requirements for the degree of

Master of Science in Mechanical Engineering

School of Mechanical Engineering

West Lafayette, Indiana

December 2019

THE PURDUE UNIVERSITY GRADUATE SCHOOL
STATEMENT OF COMMITTEE APPROVAL

Dr. Terrence Meyer, Chair
Department of Mechanical Engineering
Dr. Gregory Shaver
Department of Mechanical Engineering
Dr. Christopher Goldenstein
Department of Mechanical Engineering

Approved by:

Dr. Jay Gore
Associate Head for Graduate Studies

ACKNOWLEDGMENTS

I would like to thank my advisor, Dr. Terence Meyer for his guidance and support throughout my graduate years at Purdue. A special thank you to Cummins Inc. for the Cummins-Purdue Fellowship which gave me the opportunity to pursue my master's degree at Purdue University. I would especially like to acknowledge Mike Smyser and Conor Martin for their previous work on this topic based on which the work in this thesis is developed. I also want to thank my lab mates, Daniel Lauriola, Mateo Gomez and Austin Webb, for their technical assistance over the last two years.

TABLE OF CONTENTS

LIST OF TABLES

LIST OF FIGURES

ABSTRACT

Author: Radkar, Vaishnavi, A. MSME
Institution: Purdue University
Degree Received: December 2019
Title: Characterization and Application of a Lens System Design for Engine Diagnostics and 3D Reconstructions
Committee Chair: Terrence Meyer

A previously designed lens system is constructed and characterized for possible application to engine diagnostics and 3D reconstructions of combusting flows. Since optical engines cannot be operated at the same conditions as a production engine, optical access to a production engine, with minimum changes in the engine geometry is necessary for developing a better understanding of the in-cylinder processes. The application of a probe designed to fit in the pressure transducer port of a diesel engine was demonstrated in this work. Measurement of various optical parameters established the ability of the lens system to have a good resolution over the entire stroke length of the cylinder. The temperature analysis of the probe and lens system confirmed its ability to withstand the high-temperature conditions in the engine cylinder head. The lens system design was coupled with imaging fibers to transmit images from the image plane of the probe to a high-speed camera located at a safe distance from the combusting environment. Due to the robust design of the probe and its compatibility with an imaging fiber, the probe was identified to be a good alternative as an inexpensive lens system for tomography in challenging environments. To validate its use, 3D reconstruction of a sewing pin using a range of views was demonstrated. Parameters affecting the reconstructions were identified and optimized to obtain high-quality reconstructions.

1. INTRODUCTION

1.1 Background

The combustion process in an internal combustion engine has been of great interest to researchers for a long time. A detailed understanding of the combustion mechanism helps improve engine efficiency by ensuring complete combustion of the fuel. Nitrogen oxides (NOx), carbon monoxide (CO), carbon dioxide (CO2) and soot are the main components exhausted from any engine. Due to stringent pollution control laws, it is necessary to reduce the number of exhaust gases released in the environment. A better understanding of the in-cylinder processes, right from fuel injection to the release of exhaust gases will help reduce the amount of air polluting species being produced and released in the environment. A number of studies are thus focused on studying the process of fuel injection, the formation of a homogenous air-fuel mixture, combustion efficiency and exhaust gas treatment methods. The combustion efficiency depends on engine operating parameters such as the torque and engine speed. Thus, efforts have been made to simulate engine operating conditions to match those seen in a production engine. One of the several approaches used for such studies is the use of high-speed imaging cameras to capture several images of the in-cylinder processes, which are then analyzed to study different combustion characteristics. The non-intrusive nature of this system makes it a commonly used approach for qualitative and quantitative analysis of the engine combustion process. Studies dated back to 1960 have been using this approach to study parameters such as the start of combustion, the effect of pilot injections on combustion efficiency, etc. [1]. Along with in-cylinder visualization, the use of laser diagnostics can help determine the presence and quantity of individual species in the engine. However, optical access is needed for such recordings. A number of ways to do so are being explored. A common example is the use of an optical engine [2] in which either the cylinder wall or the piston crown is replaced by a glass window. These engines, however, cannot be run at the same operating conditions as a production engine due to the fragile nature of the glass windows being used. Thus, exploring different ways to gain optical access to a production engine is gaining importance. This study is focused on the design of an optical probe that can fit onto a diesel engine cylinder head thus providing optical access to the engine. The design considerations and the optical parameters of the lens system have been studied here.

Due to the small size and low cost of the probe, its application for three-dimensional reconstruction of flames and flows has also been studied.

1.2 Engine Diagnostics

Exhaust gas analysis helps determine the ratio and quantity of various polluting components such as NOx, CO, CO_2, O_2, and soot. Tracking the formation of these species during the combustion process can help determine the causes of their formation and develop controlling techniques. Gas sampling valves have been used to recover gas samples from the cylinder, which are then analyzed to identify the component species [3]. The sampling can be done anytime during the combustion process. However, such a process interferes with the normal operation of the engine and is not cyclically-resolved. Thus, there has been significant progress in the development of non-invasive techniques for engine diagnostics. Optical methods, especially laser diagnostics, have gained a lot of popularity since it overcomes both the difficulties mentioned above. Laser diagnostics enables the detection of minor species, the temperature of the combusting gases and can also be used to create a velocity profile for the flow [4].

Combustion of diesel results in the formation of soot. The combusting gases and soot are seen to attain a thermal equilibrium within 10^{-50} to 10^{-6} seconds [5]. After reaching thermal equilibrium the temperature difference between the combusting gases and soot particles is less than 1K [6]. Thus, temperature of the combusting gases can be obtained by measuring the temperature of soot particles. This is the basic concept behind the two-color temperature measurement method [7]. A soot particle is treated as a black body. According to Plank's law, the intensity of radiation from a blackbody depends on its wavelength and temperature. Since the radiation emitted by soot particles will be absorbed and scattered by other soot particles, the intensity of radiation from a volume containing soot particles depends on the soot density, optical path length, wavelength and temperature of the flame. The soot density and optical path length are defined by a term called KL factor, where K is the absorption coefficient proportional to the density of soot particles and L is the optical path length. The optical length can be considered equivalent to the geometrical length, but this might not always be true. As per the two-color temperature method, the flame radiation is measured at two different wavelengths and a comparison of the two intensities helps determine flame temperature and soot density along the optical path. Zhao et al. [6] have suggested the use of visible wavelengths due to the following advantages. The rate of

change of spectral emissivity of a black body with respect to temperature is higher for a visible wavelength (Figure 1) making it easy to spot the changes. Also, the spectral intensities are higher for visible wavelengths for temperatures 1000 – 2500K (Figure 1). Since the peak burning temperature attained in an internal combustion engine is of the order of 2500K [8], wavelengths in the ultraviolet range need not be considered. Thus, 550nm and 650nm were chosen as suitable wavelengths for temperature measurements [6,9].

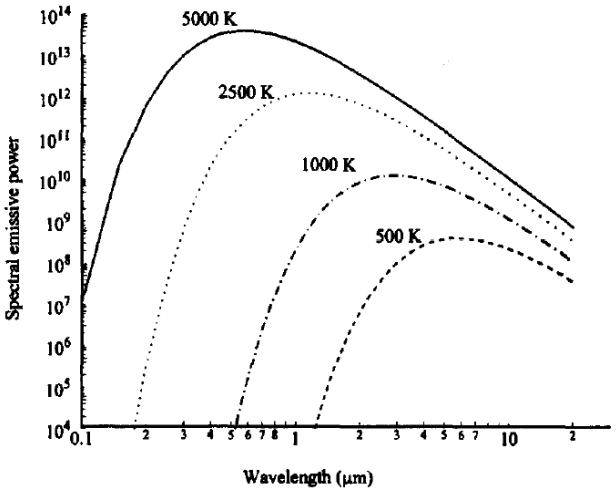

Figure 1. Spectral radiance of blackbody as a function of wavelength and temperature [6].

Besides temperature, the KL factor helps determine the soot and particulate matter density. A number of studies have utilized the two-color temperature method to determine the effects of various parameters like exhaust gas recirculation (EGR) [10], pilot injections [1], use of fuel additives, etc. on the combustion temperature and KL factor.

Since the two-color temperature studies do not need the use of external excitation, they are very popular and widely used. Another method used for soot diagnostics is the light extinction method. Here a laser is used to illuminate a measurement volume. The cloud of soot particles will absorb and scatter the light. A photodetector is placed on the other side. A comparison of the light intensity detected by the photo-multiplier with the original light intensity of the laser can be used to calculate the number of particles, their size, etc. [6].

Apart from these, certain studies also make use of external excitation to detect the presence of various species during the combustion process. Laser-induced fluorescence (LIF) is used to measure the concentration of OH and NO radicals. A suitable laser wavelength is used to excite

the radicals. As the excited particles return to their ground state, they emit radiation which is detected using an appropriate high-speed camera. [11]

The study of fuel injection, development of spray geometry, droplet formation and formation of fuel-air mixture is also important to predict the combustion efficiency. The study of the heterogeneous and optically dense region of the spray helps predict combustion instabilities and gaseous and particulate emissions. A number of methods have been developed for studying the spray characteristics. Laser extinction due to scattering and absorption of light intensity by fuel droplets can be used to determine the density and spatial distribution of droplets. Fuel is often seeded with fluorescent material which is then illuminated with the help of laser. The fluorescence emitted by these particles helps trace the development of spray parameters. [37] However, a suitable tracer has to be identified based on the type of fuel used [11].

All the diagnostic techniques mentioned above, need optical access to the engine cylinder. A number of engine modifications and geometries have been used to provide optical access to the engine without interfering with its normal operation so that the measurements obtained closely resemble the conditions in a production engine. Observation-based techniques usually require a single access point. However, for laser-based techniques, where excitation is needed, more than one access point may be needed. Depending on the requirements, different configurations have been used and studied over the years to get the best possible results. The most commonly used method is to provide optical access to the cylinder through either the cylinder head, cylinder wall, piston or a combination of these.

One of the earliest examples of an optical engine was introduced by Bowditch [1]. Figure 2. shows the modifications made to a normal engine cylinder. An elongated piston with a quartz crown was used. A slot was provided on the sides of the piton through which a mirror was housed below the piston crown. The reflection of the combustion process was studied in the mirror. This configuration was used by Bowditch to obtain images of the combustion process which were then analyzed to identify the start of combustion and the effect of pilot injections on the combustion process.

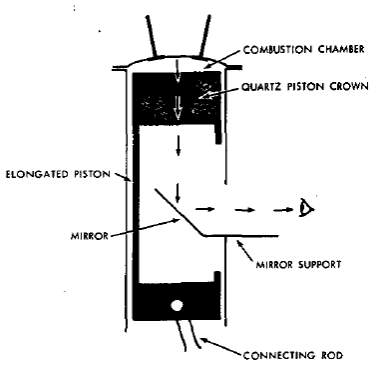

Figure 2. Optical engine with a quartz piston crown [9].

The optical engines used now are a derivative of the above design. The optical engine in Figure 3. uses the Bowditch configuration for the piston with the addition of a quartz cylinder liner for providing background illumination for laser-based diagnostic techniques.

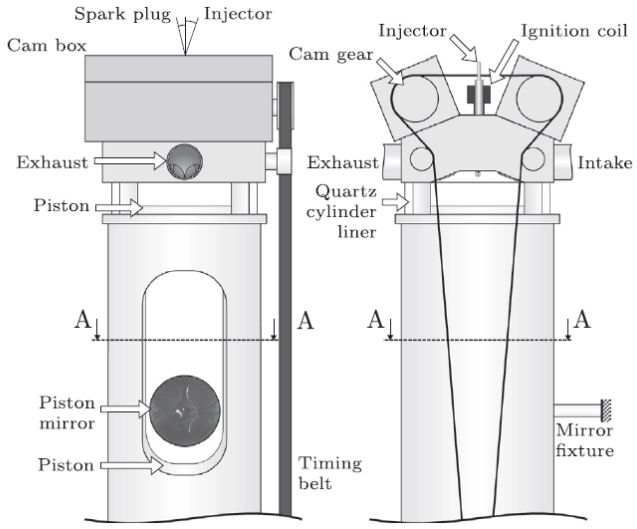

Figure 3. Single piston optical engine with quartz cylinder liner and Bowditch piston arrangement [12].

However, the engine cannot be operated at the operating conditions of a production engine since the quartz components might fracture and fail. Johansen et al. [12] used a skip fire strategy where the engine was not fired continuously but fired every few cycles. This resulted in a lower steady-state temperature than a production engine.

The use of an excitation source often needs the use of two optical access points. Dierksheide et al. [13] performed a two-dimensional (2D) particle image velocimetry (PIV) on an optical engine. PIV is used to determine the velocity field of flow by imaging an illuminated plane within the flow over a certain time interval (discussed in section 3.1.1). An optical engine with two access points along the cylinder wall was used to perform the PIV experiment. As shown in Figure 4, the laser sheet was introduced from one window and an optical window in a perpendicular direction was used for imaging purposes. However, for 2D-PIV experiments, the fuel has to be seeded with oil particles and thus, certain changes in the injection process were needed. Also, custom-designed endoscopes were used among the two optical windows. The endoscope near the laser was used to create a laser sheet and the one near the camera helped obtain a suitable field of view for measurements. Figure 5 shows the design of the endoscope. Instead of using achromatic lenses, rod lenses were used. Light gets diffracted at the glass-air boundaries and thus the use of rod lenses helped reduce the number of glass-air interfaces. As a result, a better resolution was obtained using rod lenses as compared to achromatic lenses. A comparison of the modular transfer function (MTF) for achromatic lens endoscope and rod lens endoscope is shown in Figure 4. The on-axis MTF for achromatic lens endoscope at 30% contrast is around 15 lp/mm (line pairs/mm) versus a 30 lp/mm resolution for rod lens endoscope.

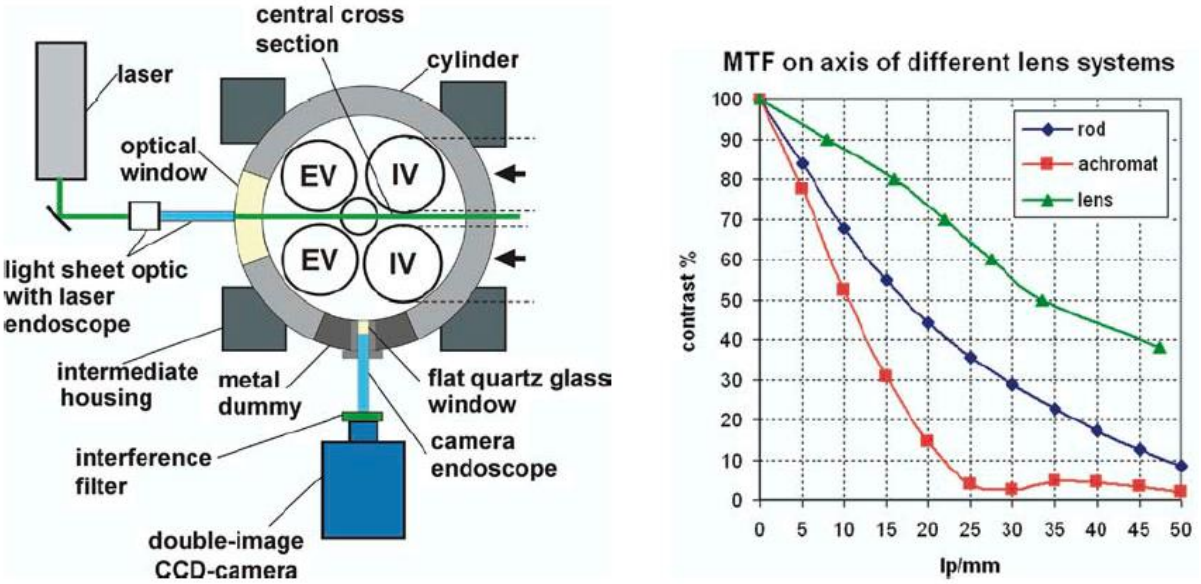

Figure 4. Experimental setup for 2D PIV experiment (left); comparison of MTF for achromatic lens and rod lens endoscope [13].

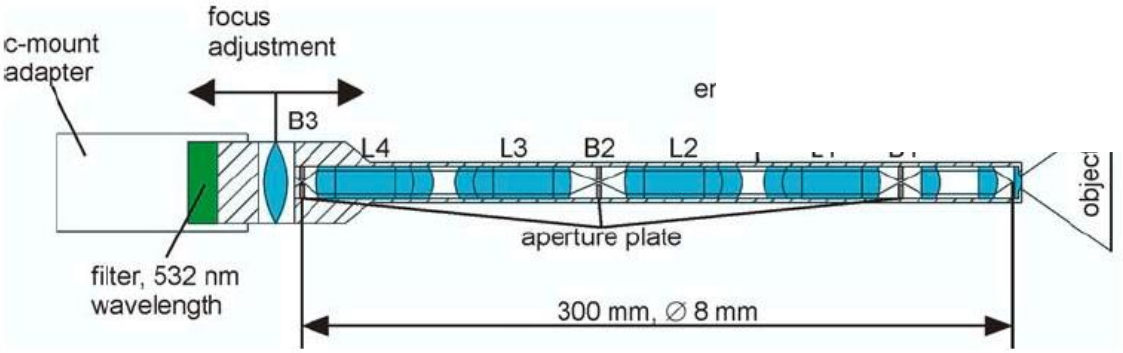

Figure 5. Design of endoscope [13].

However, the examples mentioned above required a modification in the engine geometry. Also, the operating conditions were limited due to the use of quartz components to avoid failure. The development of optical engines is costly and care needs to be taken to ensure leakproof operation. Thus, to avoid the need to change the engine geometry and obtain operating conditions as close to a production engine as possible, the use of fiber optics was explored. The concept behind these designs is similar to that of endoscopes used in the medical field. An endoscope consists of two or three optical fibers located within a single tube. The fiber optics provide flexibility to the design. One of the fiber optics carries light to the required location within the body and the reflected light is carried back through the other fiber to the eyepiece. Similarly, fiber optics are used for engine diagnostics to carry in-cylinder images from the optical window up to a camera located far away from the engine. Modifications to the image are possible near the camera thus reducing the number of optics needed to be mounted on the engine. Fiber optics being small in size, these experiments were performed on production engines with little or no changes in the cylinder geometry.

Yan et al. [14] replaced one of the two exhaust valves with a probe for optical diagnostics. A sapphire window was used to provide optical access. Sapphire has a high melting point and a high thermal expansion coefficient due to which it can sustain the harsh environment. A fiber optic was used to transmit the images from the sapphire window surface to the camera. Deposition of soot reduces the transmission quality of the probe significantly and is a major problem faced in optical diagnostics. Soot deposition is seen to have a 14% reduction in transmission at a wavelength of 0.55μm resulting in a 1% error in temperature measurements and a 5% error in soot

concentration measurements [15]. Yan et al. [14] designed the probe to be self-cleaning. The protection and restriction sleeve in Figure 6. restricted the in-and-out flow of gases. Due to the high temperature at the surface of the sapphire window, the soot particles remained dry and were blown away by the in-and-out flow of gases. However, since the probe replaced the exhaust valve, proper sealing had to be ensured and the operating characteristics of the engine were modified.

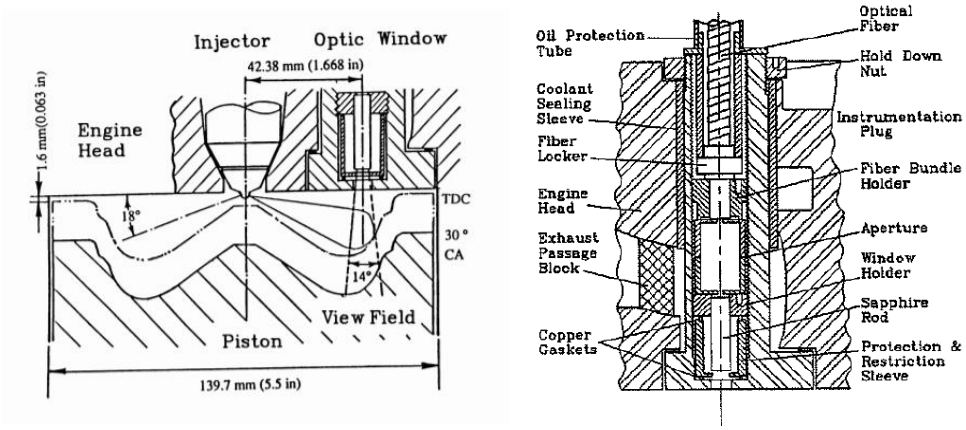

Figure 6. Position of probe next to the injector (left); design of self-cleaning probe(right) [14].

Certain gasoline engine studies include modification of the spark plug to provide optical access [16,17]. Kranz et al. [17] used fiber optics to transmit laser light into the cylinder. The spark plug was modified to house the fiber optics. (Figure 7). The piston was provided with a quartz window to provide access for the camera.

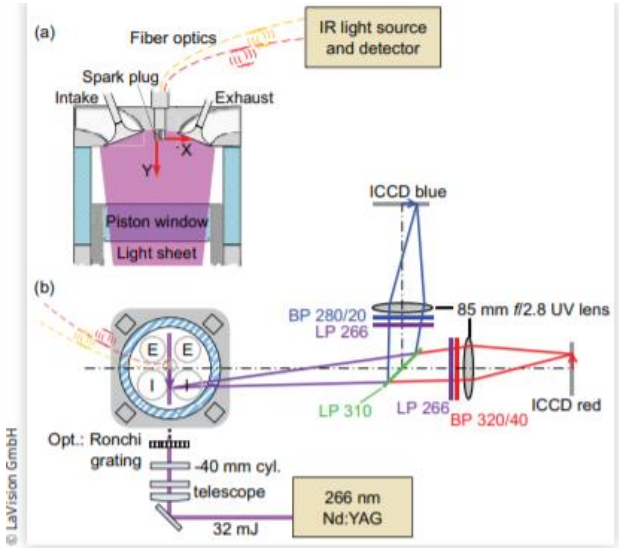

Figure 7. Modified spark plug to transmit laser light into an optically modified engine [17].

Figure 8 shows a modification in the spark plug body to house separate fiber optics to transmit light into the camera and reflected rays to the camera. Similarly, Hall et al. [18] used a modified spark plug assembly to observe and study certain pre-combustion activities

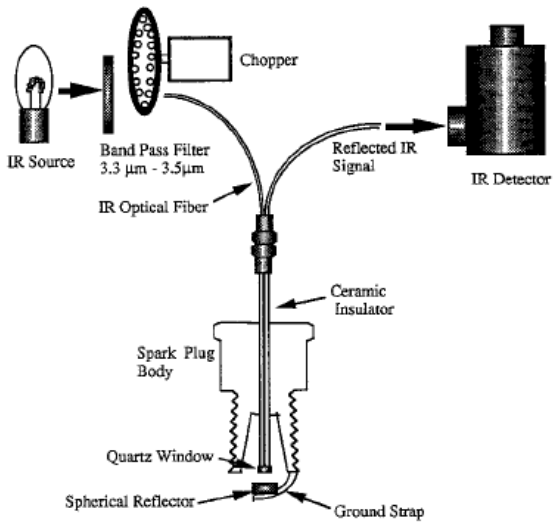

Figure 8. Modified spark plug using fiber optics to transmit light in and out of the cylinder [16].

Since diesel engines do not have a spark plug and the fuel injector cannot be modified, Shakal et al. [1] designed an optical probe to fit in the pressure transducer port of a two-stroke diesel engine. The objective of this study was to locate the start of combustion and study the effect of auxiliary injections on combustion. A sapphire window was used to provide optical access to the cylinder through the pressure transducer port. A fiber optic bundle was used to transmit images from the engine to the recording device placed far away. Since the fiber optics give a very narrow field of view certain lenses were used to obtain a field of view of 45°. The positioning of the injector was modified so that the optical probe is located between two spray plumes. The positioning of the pressure transducer port is shown in Figure 8. Certain changes were done to the piston bowl assembly to avoid the piston from hitting the fiber optic holder in the pressure transducer. To ensure proper sealing of the cylinder, copper washers were used. The holder assembly was made of SS 316 and was water-cooled. This needed certain changes to be done in the cooling system of the engine. An intensifier and image doubler were used to improve the magnification and contrast of the images obtained. Refer to Figure 9.

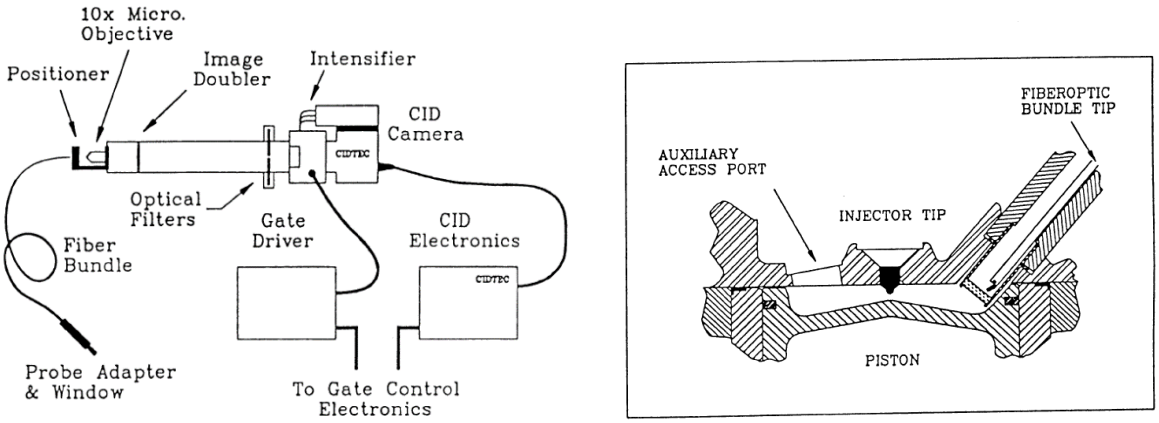

Figure 9. Components of the optical probe system (left); Positioning of the probe in the pressure transducer port (right) [1].

A similar concept was used in this study to develop an optical probe that fits in the pressure transducer port of a four-stroke diesel engine. The lens system was custom-designed for a particular engine depending on the dimensions of the engine cylinder.

2. OPTICAL PROBE FOR ENGINE DIAGNOSTICS

2.1 Position

Cummins ISB 6.7-liter diesel engine was chosen for this study. Since diesel engines do not have a spark plug, alternate locations for optical access through the engine cylinder head were explored. The main aim was to make very little or no modification to the current engine geometry. The study of the disassembled cylinder head revealed the presence of a pressure transducer in every cylinder. Figure 10 shows the position of the pressure transducer in the cylinder head and with respect to the engine exterior. Since pressure transducers do not play a vital role in the working of an engine, they can be easily replaced. Also, the pressure transducer port runs up to the cylinder wall surface and is located on the outer side of the engine making it easy to replace them with optical components. Considering the above points, the pressure transducer port was identified to be highly suitable to provide optical access to the engine cylinder. To avoid making any changes to the engine geometry the optical probe was designed according to the dimensions of the pressure transducer port.

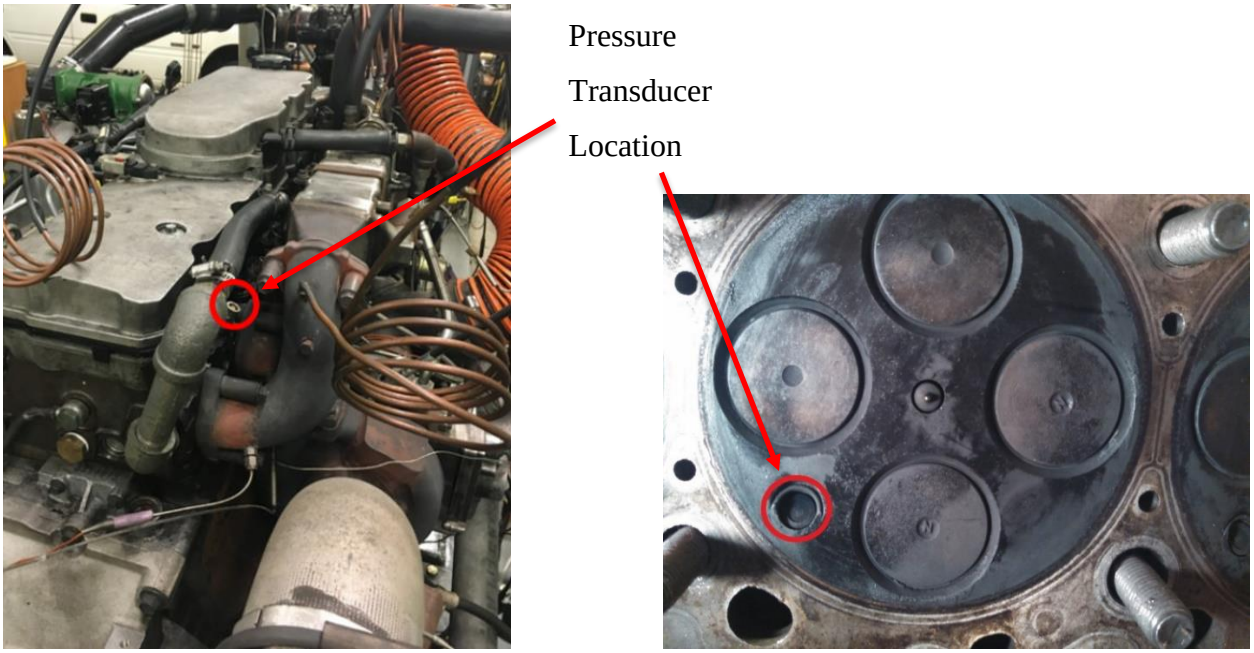

Figure 10. Location of the pressure transducer port on the engine exterior (left); and the cylinder head (right).

2.2 Design of the Probe

The optical probe was designed to address the following concerns:

1) Leakproof engine operation: The probe should fit on the cylinder head perfectly so that the engine is completely sealed off from its surroundings
2) Non-invasive: It should not interfere with the normal working of the engine.
3) Harsh environmental conditions: It should be able to sustain the high temperature and pressure conditions in the cylinder and cylinder head

The pressure transducer is housed on the lower side of a holder which screws into the pressure transducer port. The pressure transducer is designed to take pressure readings without interfering with the normal operation of the engine. Thus, to address the first two design concerns, the optical probe was modeled exactly similar to the pressure transducer housing. Figure 11. Shows the necessary dimensions.

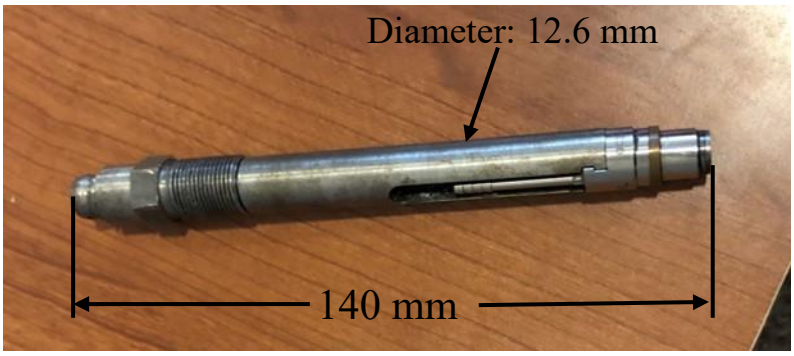

Figure 11. Dimensions of the pressure transducer housing.

2.2.1 Design of the Lens System

The most important aspect of the probe was the design of the lens system. The lens design was based on the following considerations:

- Good resolution over the entire stroke length of the cylinder
- Sizes of optics and spacing between them limited by the pressure transducer port dimensions
- Focusing a larger field of view on a small image plane
- Transmitting the image from the image plane to a high-speed camera located away from the engine

The lens design shown in Figure 12. was found to address all the above points. The lens design was created using Zemax, software for visualizing lens design and ray tracing. *The lens system design was done by Mike Smyser*.

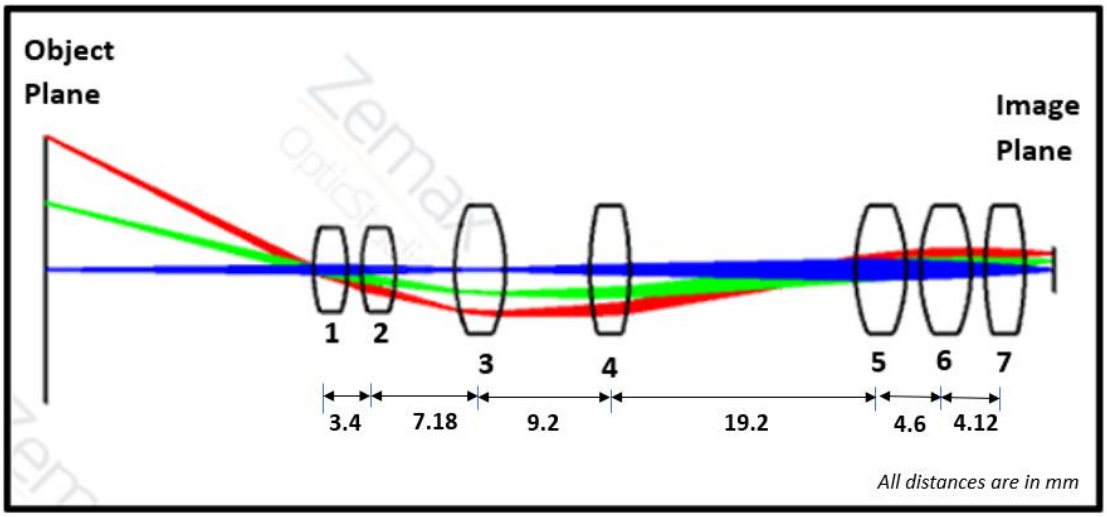

Figure 12. Ray diagram for the optical system (object distance: 19mm).

Table 1. Specifications of the lenses.

Sr. No.	Lens Type	Material	Diameter	Focal Length	Wavelength Range
1	Bi-convex Lens	N-BK7	6 mm	10 mm	350 nm - 2.0 μm
2	Bi-convex Lens	N-BK7	6 mm	10 mm	350 nm - 2.0 μm
3	Bi-convex Lens	N-BK7	9 mm	12 mm	350 nm - 2.0 μm
4	Bi-convex Lens	N-BK7	9 mm	20 mm	350 nm - 2.0 μm
5	Bi-convex Lens	N-BK7	9 mm	12 mm	350 nm - 2.0 μm
6	Bi-convex Lens	N-BK7	9 mm	12 mm	350 nm - 2.0 μm
7	Bi-convex Lens	N-BK7	9 mm	20 mm	350 nm - 2.0 μm

As seen from Table 1., the size of the optics was limited to 9mm so that they fit in the pressure transducer hole. Lenses used for the design are commercially available. As discussed in section (1.2), visible wavelengths are used for most of the diagnostics imaging. Thus, the lens material was chosen such that it has 90% transmission in the visible region of the spectrum. (Figure 13.)

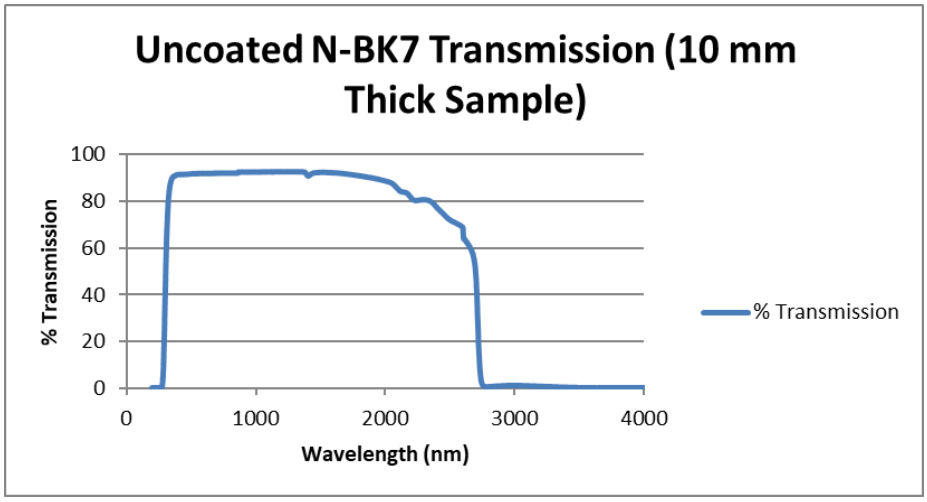

Figure 13. Transmission data for N-BK7.

Lens-to-lens distance is shown in Figure 12. Since the distances are so small, it was practically difficult to maintain such close distances. Thus, lens distance was changed to see the effect on image formation using Zemax. It was observed that changes in the distances by a couple of millimeters did not affect the image formation except for the distance between the last two lenses. An increase in the distance between the last two lenses caused the image plane to coincide with the last lens. Also, it is not desirable to change the total axial length of the system. Thus, the lens distances were chosen such that the total axial length remains the same. Figure 14 shows the ray diagram for random distances.

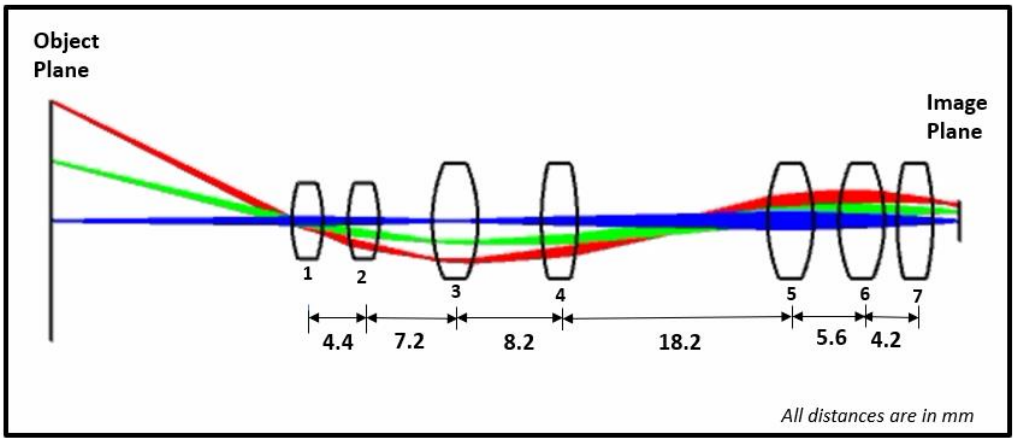

Figure 14. Ray diagram for random lens distances.

Section (2.3) will provide a detailed discussion about the practical testing of the probe, determination of various parameters and comparison with simulation results.

2.2.2 Temperature Considerations

To develop a probe, such that it fits in the pressure transducer port perfectly and seals the passage so as to avoid any leaks, an outer covering was designed for the lens system. Also, spacers were designed so as to maintain the correct distance between the lenses as specified in the design. Figure 16 shows the exploded view of the proposed probe design. *The design of various probe components was done by Conor Martin.*

Figure 15. Proposed probe design.

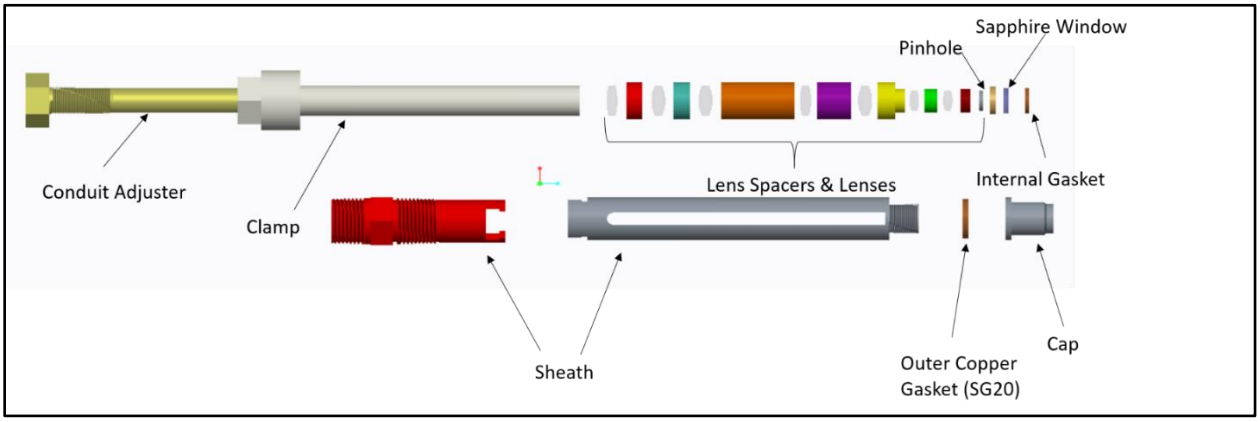

Figure 16. Exploded view of the probe.

Figure 16 shows that a sapphire window is used at the tip of the probe. This is because sapphire has high strength and temperature resistance. It will also protect the lens system from soot or any flying material. Moreover, Sapphire has an excellent transmission from Ultraviolet to mid-Infrared range [35].

The most important consideration while choosing the materials for the various components of the probe is the high-temperature environment the probe will be exposed to. The pressure transducer used in the engine is water-cooled. Due to the complex design of the probe and availability of limited space, it is not possible to provide additional cooling to the probe. Thus, the

only source of cooling available is heat transfer to the cylinder wall surface through contact and the environment. Thus, the materials need to be chosen very carefully so that they can withstand the high temperature and pressure inside the engine cylinder without causing any damage or disruption to the engine.

A temperature analysis was done to approximately predict the temperature range to which the probe will be exposed along the length of the cylinder wall. A number of studies have been done to measure the temperature of the cylinder head and valve surfaces experimentally as well as computationally.

Analysis of the cylinder head and the exhaust valve surface was done to determine the effect of interaction between the exhaust valves and the cylinder head on exhaust valve stresses [19]. A detailed finite element model was developed for a 14-cylinder diesel engine cylinder head. The results obtained from the finite element method were verified by comparing with experimental results. A number of thermocouples were positioned at different locations in the cylinder head as shown in figure 17. Since the pressure transducer port is located between the exhaust and intake valve, the temperature readings of points 2, 8 and 6 were considered. Figure17 shows the comparison between experimental and computational values of temperature at various points. It can be seen that the temperature measured at these points lies between 250 and 300° C. For design purposes, the higher of the two values was considered, i.e. 300°C.

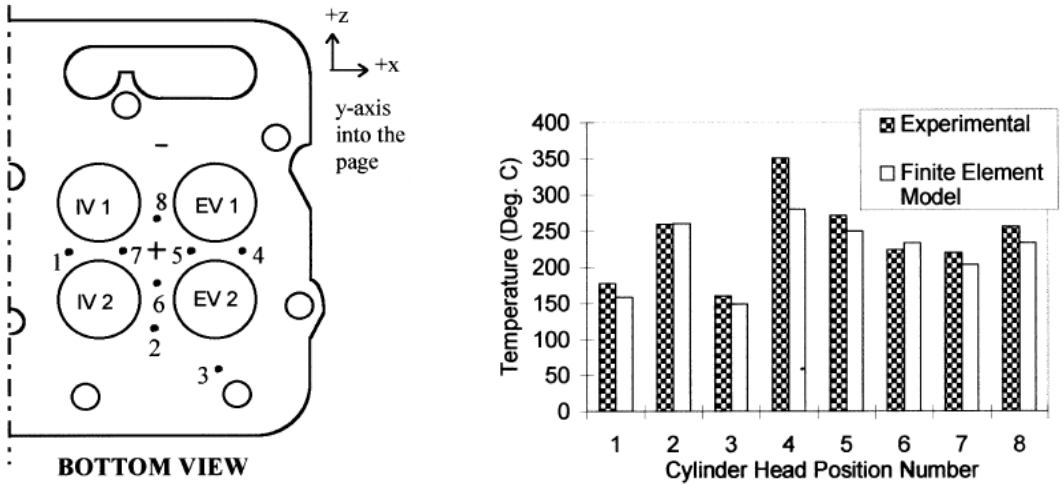

Figure 17. Position of thermocouples (left); measured temperatures (right) [19].

Similarly, Divis et al. [20] placed a number of thermocouples 18 mm away from the cylinder wall surface to estimate heat transfer through the cylinder head. The positions and the

measured temperatures are shown in Figure 18. Point 3 was identified as the point of interest. A temperature of 169°C (442K) was recorded at that point. However, the measurements were made 18 mm away from the cylinder wall surface. Thus, this value cannot be considered as the true representation of the cylinder wall surface temperature near the fire deck. The authors also suggested that due to high engine speed and thermal inertia of the various components in the cylinder head, temperature variations can be considered to be damped out within 1 mm of the surface. Thus, it was assumed that the temperature in the range of 170°C can be expected away from the cylinder wall surface.

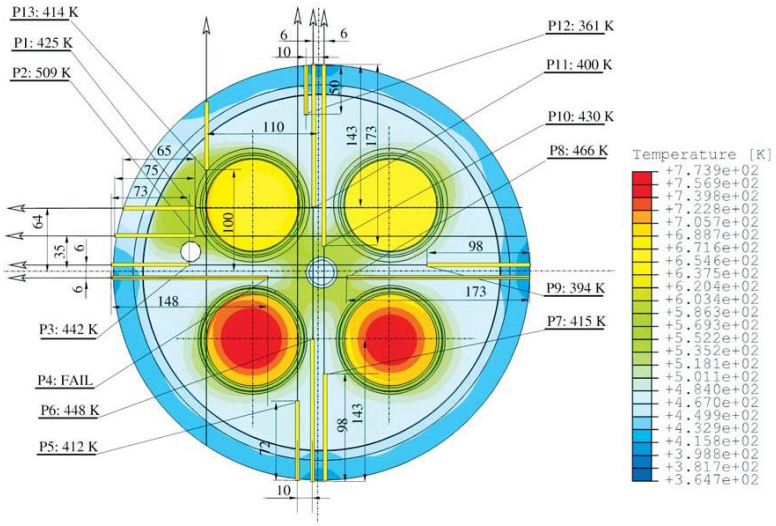

Figure 18. Measured temperatures at various points along the engine cylinder head [20].

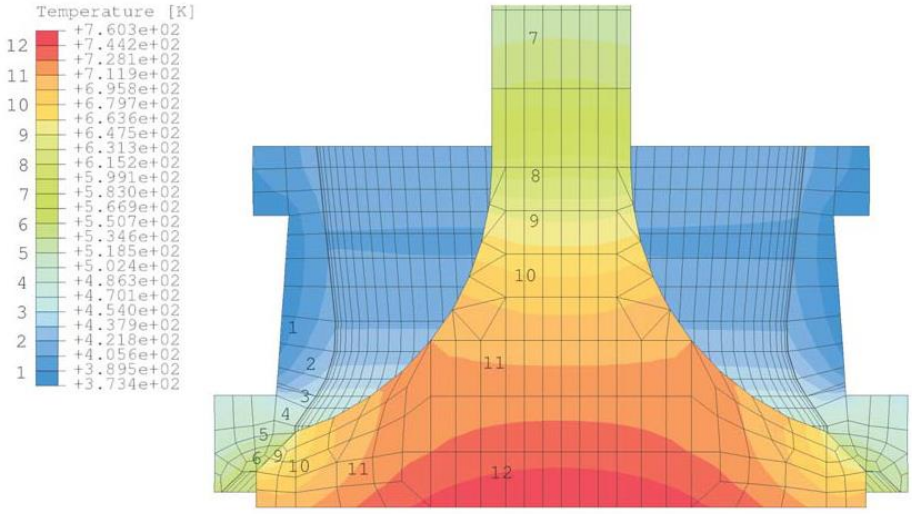

Figure 19. Temperature distribution along the exhaust valve surface [20].

Figure 19 shows the temperature distribution in the exhaust valve. A finite element model predicted the temperature at the tip of the exhaust valve to be around 760.3K, i.e. 487°C. Since exhaust valves come in contact with hot exhaust gases every combustion cycle, it was considered that the temperature of the probe tip will not be more than the temperature of the exhaust valve. Also, the surface area of the probe tip is much smaller. Hence it was considered safe to assume that the temperature at the probe tip will be less than 487°C.

Another point of consideration is that the above analysis was performed for a much larger engine as compared to the one for which the probe has been designed. Thus, the actual temperature values might be lesser than the ones measured in the above studies.

Also, the data available from the Cummins ISB 6.7-liter engine in the test cell shows that the temperature at the cylinder wall can be assumed to be 400°C. Based on the discussion above estimation of the temperatures around the pressure transducer port was done. Figure 20 summarizes the expected temperatures at various points.

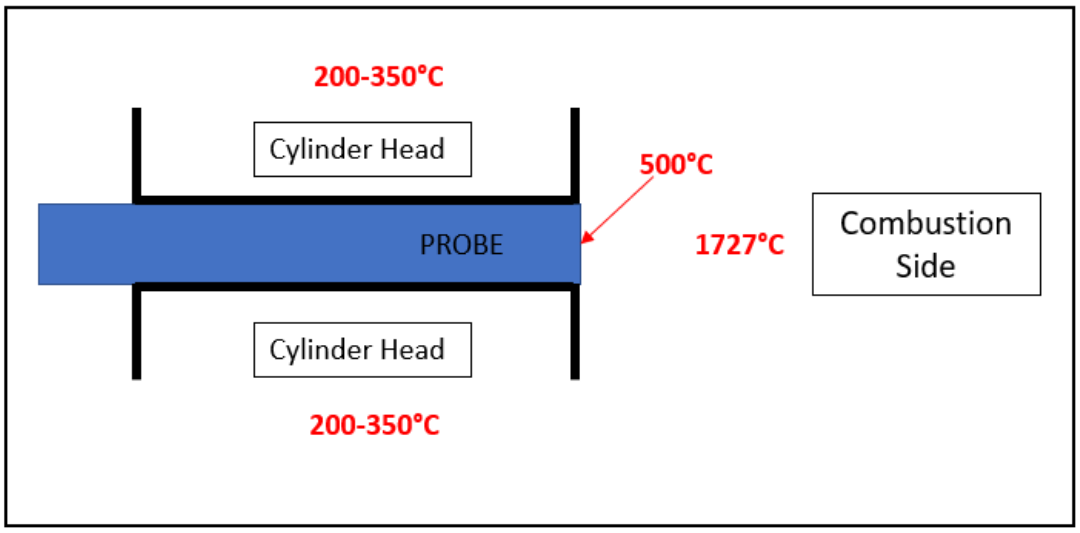

Figure 20. Temperature Summary.

Before selecting materials for the probe, a material analysis was performed on the original pressure transducer and its housing on a Scanned Electron Microscope. The test provided the elemental composition and percentage distribution for each test piece. The results were compared with commercially available materials to identify the material used for pressure transducer and housing respectively.

Table 2. Elemental composition of pressure transducer.

Point	Fe	Mn	Cr	Mo	Al*	Ni*
1	69.48	0.79	14.75	1.6	0.78	6.19
2	71.54	0.86	15.17	1.4	0.55	5.41
3	70.6	0.82	15.05	1.47	0.64	5.86
4	72.72	0.91	15.46	1.14	0.35	4.62
5	69.25	0.81	14.74	1.3	0.49	4.95
6	69.96	0.83	14.95	1.53	0.73	6.23

Element	**Fe**	**Mn**	**Cr**	**Mo**	**Al**	**Ni**
Mean (%)	**70.59167**	**0.836667**	**15.02**	**1.406667**	**0.59**	**5.543333**

* more than 5% error

The elemental composition of the pressure transducer closely resembles that of stainless steel. All stainless steels have at least 10.5% chromium. Type 316 closely resembles the composition seen in table 2. Also, type 316 stainless steel is commonly used in the construction of exhaust manifolds and heat exchangers since their melting range is 1371-1399°C. Shakal et al. [1] used SS 316 for their optical probe.

Table 3. Elemental composition of pressure transducer housing.

Element	**Fe**	**Mn**
Weight %	**96.27**	**1.73**

The elemental composition of the housing suggests that the material used is carbon-manganese steel. The sealing surfaces in an engine are usually made of chromium and manganese since they need high-temperature resistance and durability. Thus, carbon-manganese steel can be used for sealing surfaces. Based on the discussion above following materials were chosen for different parts of the probe, based on their position and functions (Table 4)

Table 4. List of probe parts and suggested materials.

Part Number	Name	Material	Quantity	Melting point (K)
1	Top Sheath	SS 316	1	1644-1672
2	Bottom Sheath	SS 316	1	1644-1672
3	Cap	SS 316	1	1644-1672
4	Conduit Adjuster	SS 316	1	1644-1672
5	Final spacer	SS 316	1	1644-1672
6	Inner Gasket	Copper/Brass	1	1358/1173-1273
7	7th Spacer	Copper/Brass	1	1358/1173-1273
8	6th Spacer	Copper/Brass	1	1358/1173-1273
9	5th Spacer	Copper/Brass	1	1358/1173-1273
10	4th Spacer	Copper/Brass	1	1358/1173-1273
11	3rd Spacer	Copper/Brass	1	1358/1173-1273
12	2nd Spacer	Copper/Brass	1	1358/1173-1273
13	1st Spacer	Copper/Brass	1	1358/1173-1273
14	Lenses	N-BK7	7	830
15	Sapphire window	sapphire	1	2323
16	Copper Spacer	Copper	1	1358
17	Outer Gasket	Copper	1	1358

The probe is designed such that the inner gasket is facing the combustion chamber. Sapphire window is the next in line. The entire lens system will be positioned behind the sapphire window. Sapphire has a very high melting temperature (2323K/ 2050°C). The inner gasket will be made of copper or brass. Both the materials have a melting temperature higher than 1000°C.
From the available literature, the temperature of the cylinder surface will not be more than 350°C and that at the probe tip can be assumed to be 480°C. This can lead to conductive heat transfer from the probe to cylinder walls further reducing the probe temperature.

Even if we consider a temperature of 480°C, the inner gasket and the sapphire window (the two parts directly in contact with the gases) have a low probability of damage since they have a much higher melting point. Also, since the 1st lens is around 6 mm away from the probe tip the temperature at the lens can be expected to be much lower than 830°C. Thus, we can theoretically assume that the probe parts would be safe in the high-temperature environment.

Another point of consideration is the high-pressure environment in which the probe will be used. The melting point of material increases with increasing pressure. An increase in pressure will suppress the volumetric expansion in solids. Thus, higher energy would be required to melt the solid. Thus, the melting points for the probe parts will be higher than the ones shown in Table

5. As a result, it is safe to assume that the probe will be able to withstand the high temperature and pressure environment in the engine.

The spacers are made of copper due to its malleable nature. Also, since the spacers are in contact with the lenses a softer material is needed to avoid scratching of the lenses.

2.2.3 Fiber Optics

The total axial length of the imaging system (considering only the lenses) is around 50mm. The pressure transducer port is 140 mm long. Thus, to image directly from the image plane, the camera will have to be focused 90 mm inside the engine cylinder surface. Also, due to the availability of limited space around the engine, it might be difficult to position the camera right next to the engine. Thus, as discussed in section 1.2, the use of fiber optics along with the probe was incorporated in the design. One end of the fiber optic was placed at the image plane and the other end at the focal point of the camera. To adjust the position of image conduit according to the image plane location a conduit adjuster was included in the design of the probe (Figure 16)

2.3 Practical Testing of the Probe

To test various properties of the probe, a probe was built using the parts listed in Table 5. All the parts are manufactured by the optical equipment company, Thorlabs.

Table 5. Part used for building the optical probe.

Part Name	Type	Specifications	Quantity
LB1157	Bi-convex Lens	Ø6.0 mm, f = 10.0 mm	2
LB1494	Bi-convex Lens	Ø9.0 mm, f = 12.0 mm	3
LB1212	Bi-convex Lens	Ø9.0 mm, f = 20.0 mm	2
SM05L30C	Slotted Lens Tube	Ø1/2", 0.535"-40 Thread, 3" Thread Depth	1
LMRA6	Lens Adapter	Ø1/2" Adapter for Ø6 mm Optics	2
LMRA9	Lens Adapter	Ø1/2" Adapter for Ø9 mm Optics	5
SM05RR	Retaining Rings	SM05 Retaining rings for Ø1/2" Lens Tubes	7

The most important aspect of the probe building was maintaining appropriate distances between the lenses as per the design discussed in section (2.2).

Since the diameter of the image plane is very small, a camera with a small chip size was needed to test the optical design. PointGrey Chameleon 2.0 CCD camera was used for the testing. It has a pixel size of 3.75µm and offers high-resolution imaging capability. A long-distance microscopic lens (InfiniMax MX-4) was attached to the camera. The objective lens offers a magnification of 1.16X and has a working distance of 181-164 mm. Along with the microscopic lens, the camera offers a resolution of 291pixels/mm. A business card was imaged with the probe and camera setup, as shown in Figure 22, to test the working of the lens design. As seen in Figure 23 the image obtained had good resolution and contrast. The image plane was seen to have a diameter of 2.8mm.

Figure 21. Assembly of the optical probe.

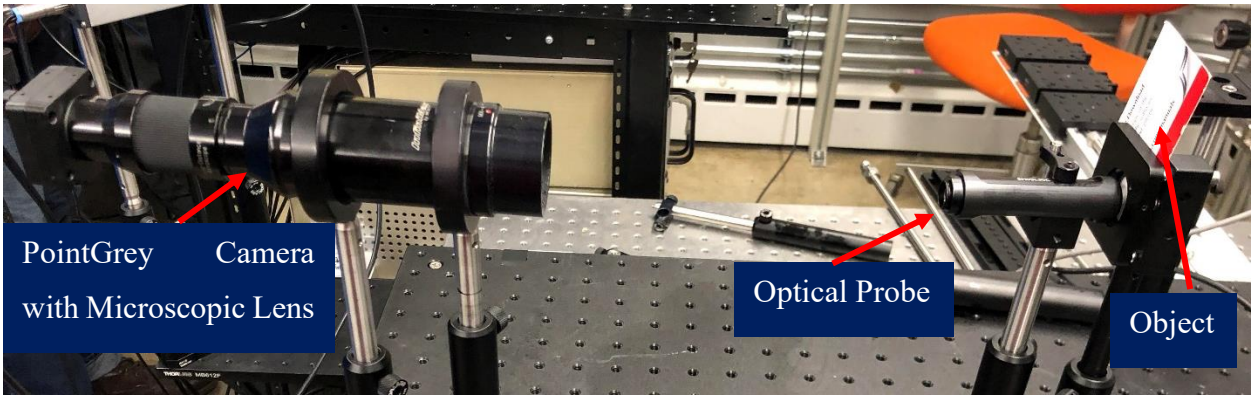

Figure 22. Experimental Setup.

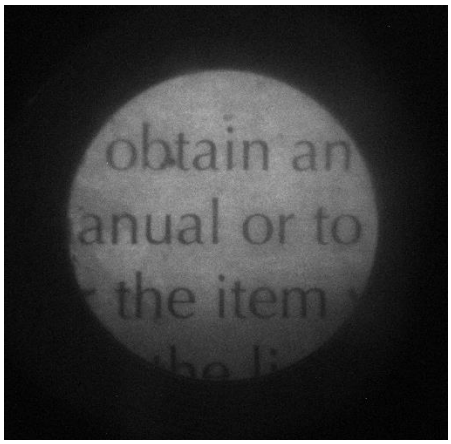

Figure 23. Obtained image.

To quantify various optical parameters like resolution, contrast and modular transfer function (MTF), the 1951 air force target was imaged. The results obtained were compared with the results of Zemax.

2.3.1 Resolution

The modular transfer function (MTF) is used for comparing various optical systems. It is defined as the ability of an imaging system to transmit contrast at a particular resolution from an object to the image [21]. MTF plots were generated for two object distance, 15mm and 50 mm. The probe was seen to have a resolution of 13.92 lp/mm (line pairs/mm) at 30% contrast for an object imaged at a distance of 15 mm (Refer Figure 24) and 7.8 lp/mm at 25% contrast for an object imaged at 50 mm (Refer Figure 25). 7.8 lp/mm lies between the resolution of group 2 elements 6 and group 3 elements 1. Similarly, for a distance of 15 mm, 13.92 lp/mm lies between group 3 element 5 and group 3 element 6 which are the smallest visibly distinguishable groups.

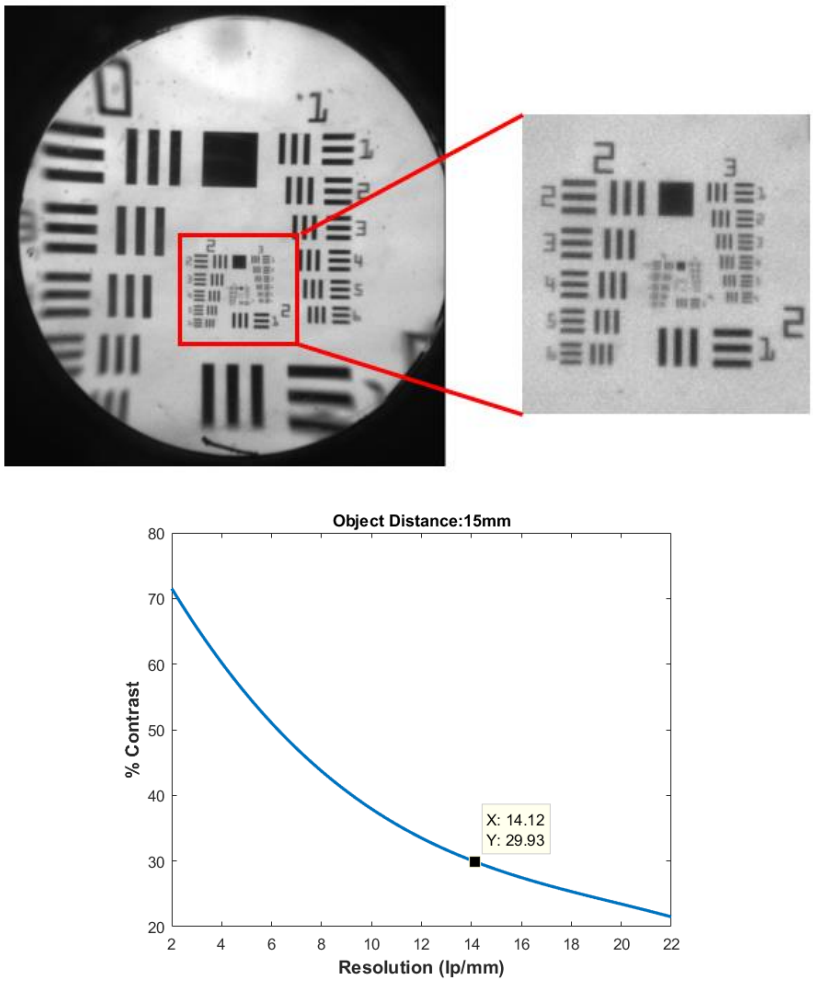

Figure 24. Test target image for object distance 15mm (top); MTF plot (bottom).

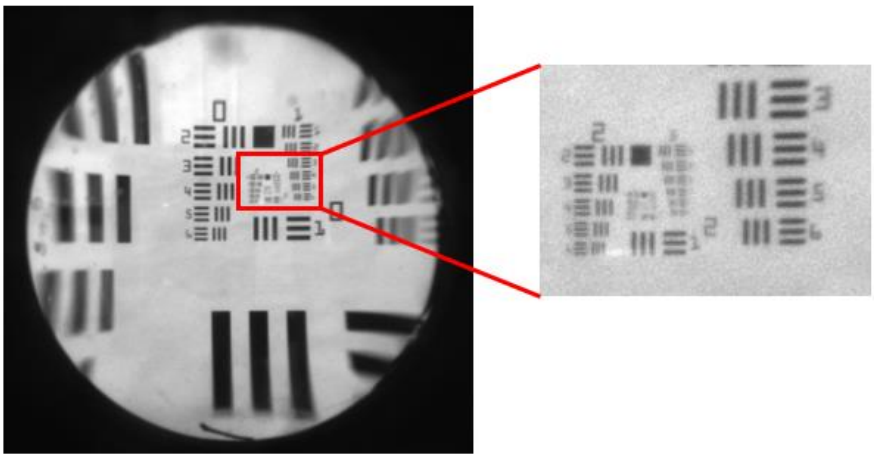

Figure 25. Test target image for object distance 50 mm (top); MTF plot (bottom).

Figure 25 continued.

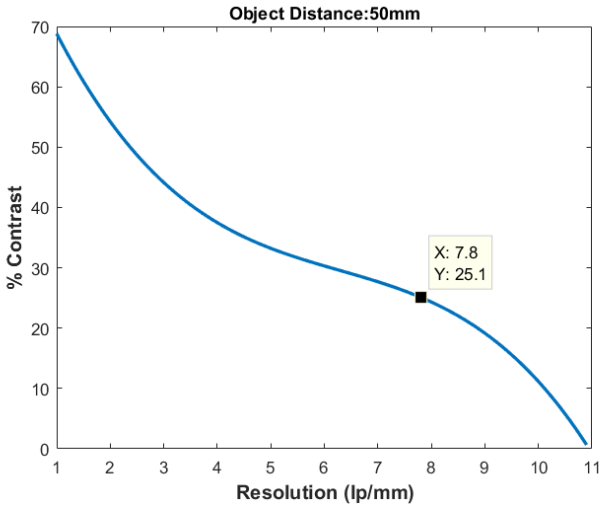

MTF plot obtained from Zemax for an object distance of 15mm is shown in Figure 26. The resolution at 30% contrast was seen to be 15.86 lp/mm off-axis and 63.8 lp/mm on-axis. The MTF of the system obtained experimentally was lower than the computed value, since MTF calculation for the entire system includes the effect of camera and lens along with the probe. Also, since the probe was built by hand, there might be a slight difference between the actual and the required lens distances.

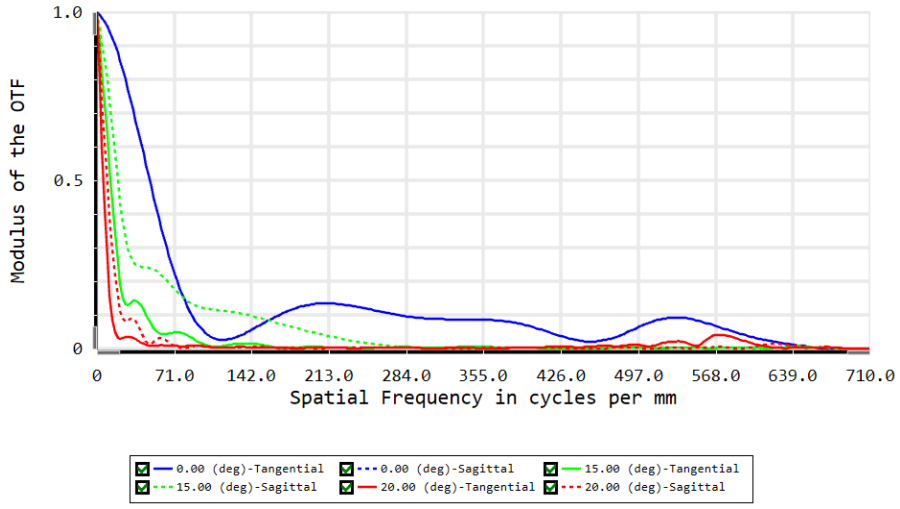

Figure 26. MTF graph for optical system obtained in ZEMAX (object distance 15mm).

2.3.2 Image Plane Position and Depth of View

The lens design analysis on Zemax indicated that the image plane distance changes with the object distance. Table 6 indicates the position of the image plane for various object distances.

Table 6. Variation in image plane distance with object distance.

Object Distance (mm)	**Image Plane distance (mm)**
10	2.1
20	1.9
30	1.8
50	1.7
100	1.65
124	1.65
500	1.65
1000	1.5

Further analysis indicated that an image plane distance of 2.1 mm can be used for shorter object distance (up to 60m) and 1.7mm can be used for object distances beyond 50mm. This was verified experimentally by imaging a test target at different distances from the probe while keeping the image plane position constant. When the image plane was fixed at 2.1 mm it was observed that the resolution of the system reduced and became unacceptable beyond 60mm. Figure 27 shows the test target image for an object distance of 60mm with the image plane 2.1 mm away from the last lens. Similarly, the image plane was kept constant at 1.7mm and the test target was imaged at different object distances. The test target image at 15mm had reduced clarity, especially near the optical axis. A plot of resolution at 30% contrast for varying object distances is shown in figure 27. The probe was seen to have a resolution above 2lp/mm up to 150 mm. Thus, it was concluded that the probe had a depth of view of 130mm. The stroke length for the engine is 124mm. Thus, the probe will have an excellent resolution over the stroke length. Table 7 shows the values of resolution and field of view for different object distances.

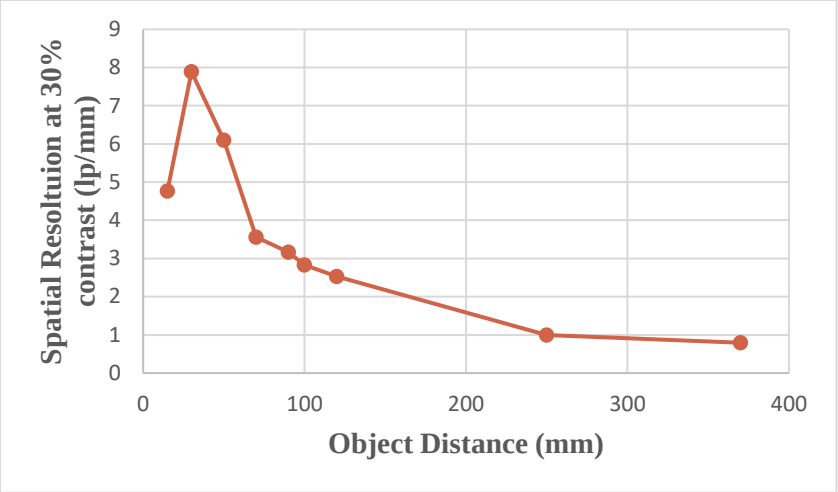

Figure 27. Variation of resolution with object distance.

Table 7. Resolution and field of view.

Object Distance (mm)	Resolution at 30% contrast (lp/mm)	Field of View (mm)
15	4.765	18.032
30	7.89	31.425
50	6.1	46.805
70	3.56	57.97
90	3.17	80.35
100	2.83	85.804
120	2.53	107.58
250	1	243.705
370	0.794	361.43

2.3.3 Aberrations

Aberrations affect the quality of the image obtained and deteriorate the MTF of an optical system. It is thus essential to identify the types of aberrations affecting the optical system in use. Aberrations can be broadly classified into two types: chromatic and achromatic aberrations. Chromatic aberrations are caused when different wavelengths travel at different speeds causing different colors to be focused on different planes. Monochromatic aberrations are related to the lens geometry at a single wavelength. These are also called as Seidel aberrations and are classified into five types, namely, distortion, astigmatism, spherical aberration, coma and curvature of field. They are the easiest to identify and correct.

Spherical aberration is caused when the shape of the lens being used is not perfectly spherical. This causes the rays of light passing through different parts of the lens to not focus at a single point. This kind of aberration only affects the rays of lights originating from a point on the optical axis. Coma is a type of aberration affecting the rays originating from off-axis points. Similar to spherical aberration, the rays originating from a common point may not focus at one point after passing through the lens. Astigmatism affects rays of light originating from a point off-axis. In this case, the rays view the lens to be tilted. This causes the rays to come in focus at different distances from the lens resulting in a blurry image. Curvature of field is caused when the rays of light are brought to focus along a curved path after passing through the lens. In the case of distortion, the points of focus in the image plane are at a different distance from the optical axis as compared to their corresponding distances in the object plane. Figure 28 illustrates the different types of aberrations.

Distortion is further divided into two types. When the points in the field of view appear further away than normal it is called positive of pin-cushion distortion and when they appear closer to the center it is called Barrel of negative distortion. Figure 29. shows the effect of both distortion types. [22,23,24]

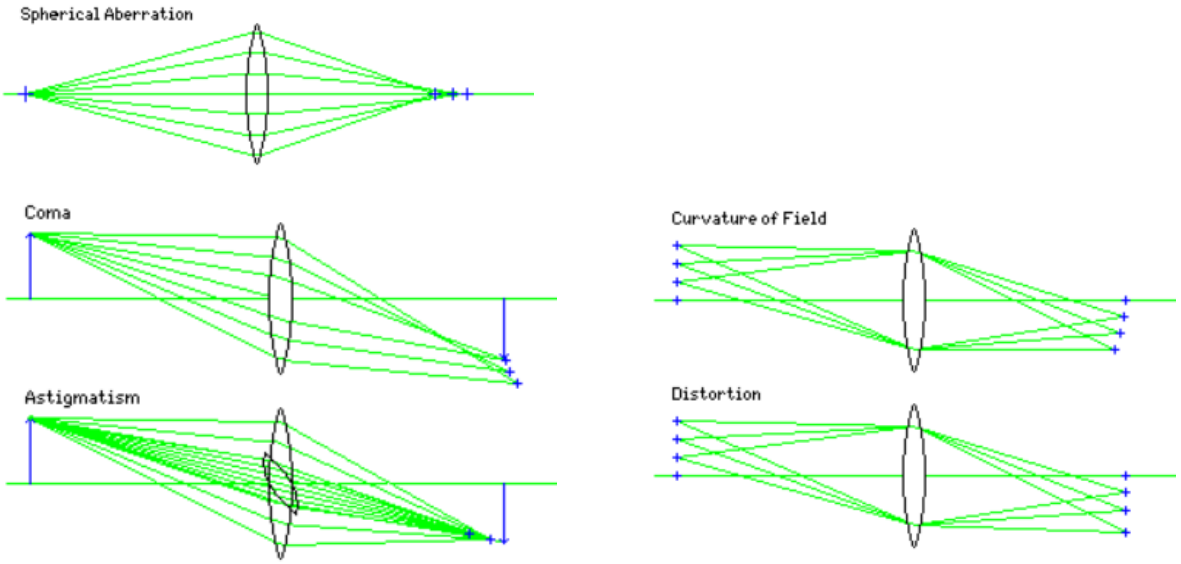

Figure 28. Ray diagram showing different types of aberrations [22].

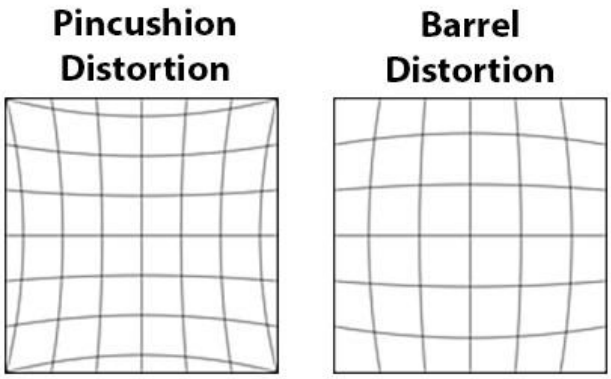

Figure 29. Types of distortion [24].

Each seidel aberration can be identified by wavefront coefficients and has a formula associated with it which helps in the quantification of each aberration. These equations are used to identify the contribution of the individual surface aberrations relative to each other. A graphical representation of this is called a seidel diagram and is commonly used in the designing of an optical system.

Figure 30 shows the Seidel diagram created on Zemax for the optical system. Distortion is seen to be the most prevalent aberration followed by Curvature of field and astigmatism. The values of various wavefront coefficients have been shown in Table 8.

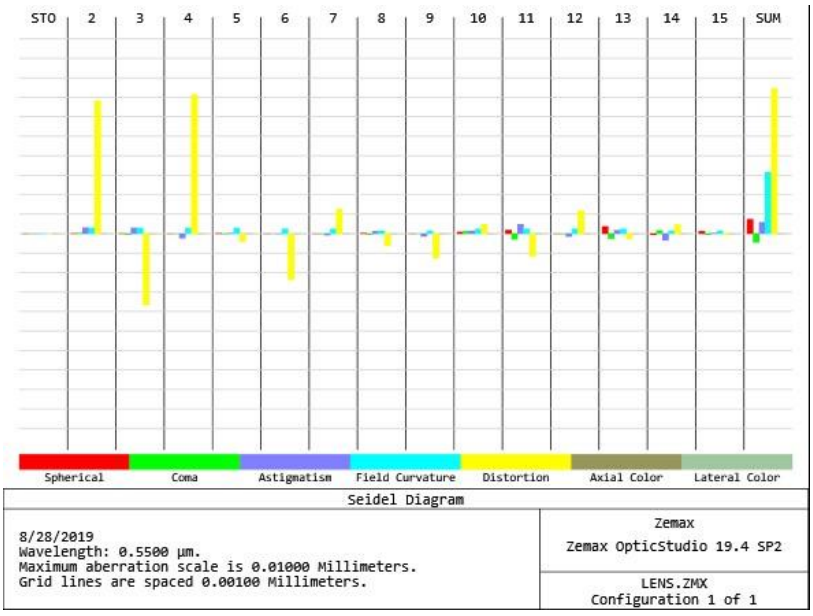

Figure 30. Seidel diagram.

Table 8. Values of seidel coefficients.

Aberration	Seidel Coefficient	Value
Tilt	W111	0.7638
Defocus	W020	-0.9444
Spherical	W040	0.168
Coma	W131	-0.421
Astigmatism	W222	0.5347
Field Curvature	W220	1.434
Distortion	W311	6.7798

These aberrations were practically observed in the images obtained using the optical probe. Figure 31 shows the image of a calibration target 150 mm away from the lens system. The corners of the image are stretched upwards clearly showing pin-cushion distortion and curvature of field. A distortion test target was imaged to quantify the distortion percentage. Distortion percentage was measured by comparing the distance of points at various image heights (predicted distance) with the ideal distances (actual distance) provided by the manufacturer.

$$Distortion\ \% = \frac{Actual\ Distance - Predicted\ Distance}{Predicted\ Distance} \times 100$$

The graph in Figure 32 follows the trends of pin-cushion distortion with a 7% distortion at a height of 13mm. Since distortion is a third-order aberration, its value is dependent on the cube of the image height. Thus, the image quality at the corners of the probe is further degraded. The experimental and Zemax based distortion measurements have been done for an object distance of 40 mm.

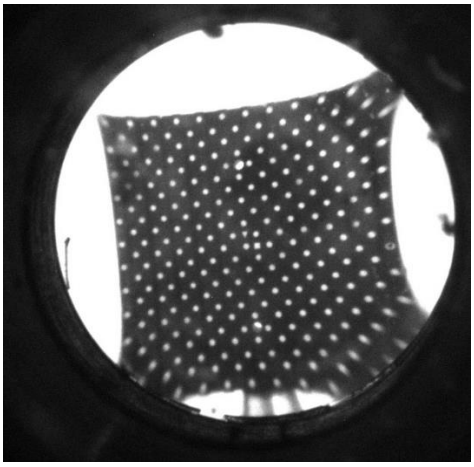

Figure 31. Distorted calibration test target.

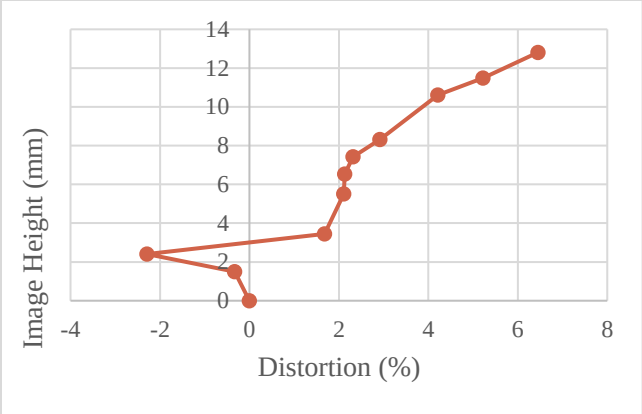

Figure 32. Variation of distortion with image height.

2.4 Use of Imaging Fibers

As discussed in section 2.2.3, the use of fiber optics to transmit images over long distances was explored. Fiber optics are bundles of fibers that transmit light from one end to the other by the principle of total internal reflections. In this study, the use of two types of fiber optics was explored. Table 9 gives the specifications of the two imaging fibers used for testing:

Table 9. Specifications of imaging fibers.

	No of elements	Fiber Diameter (μm)	Outer Diameter (mm)	Length	Wavelength Range (nm)	Flexibility
Image Conduit	50,419	12	3.2	152.4 mm	400-750	No
Optical Fiber	30,000 +/- 3000	2000 ± 150	1.85 ± 0.5	3 meters	400-750	Yes

1) Image Conduit: Image conduit is a glass tube of relatively short length supplied by Edmund Optics (maximum available length 305 mm). It is possible to change its shape at a temperature of 700°C. However, at room temperature, it is not flexible. Thus, the probe, image conduit and the camera need to be aligned along one axis. The air force test target was imaged using the combination of probe and image conduit to compare the quality of the image obtained. One end of the conduit was placed exactly at the image plane and the other end was imaged on the PointGrey camera. Loss of light over the length of the image

conduit results in reduced resolution as compared to the probe. A combination of image conduit and the probe were observed to have a resolution of 4.904 lp/mm at 30% contrast.

2) Optical Fiber: The optical fiber used was 3 meters long and flexible. Due to its flexibility, the optical fiber can be used when there are space constraints and the camera cannot be placed along the same axis as the object and the probe. However, since the image had to travel along a longer distance, the loss in light intensity was higher resulting in reduced contrast and resolution. Also, lesser number of fibers affected the quality of the image giving a resolution of 2.145 lp/mm at 30% contrast.

Figure 33. shows a comparison of the modular transfer function (MTF) plots of the three combinations, namely, probe, probe + image conduit, and probe + fiber optic.

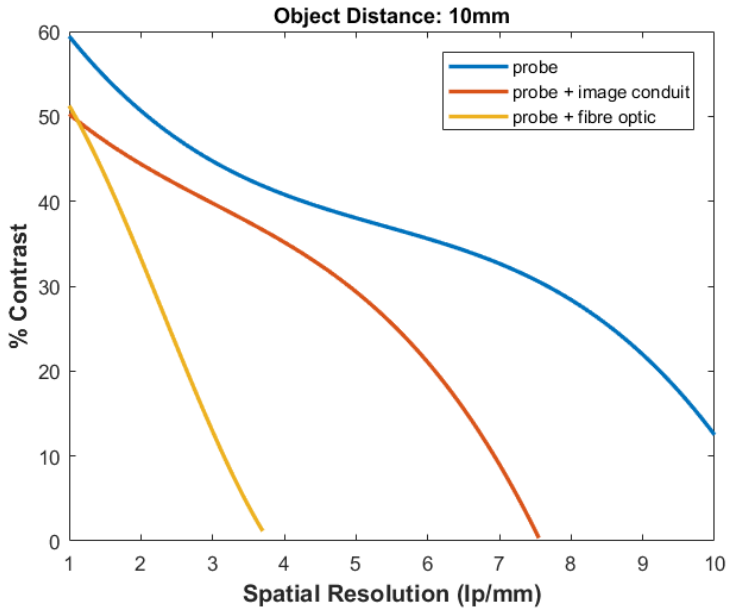

Figure 33. Comparison of MTF for probe, image conduit and fiber optic with object distance 10mm.

Table 10. MTF values at 30% contrast.

	Resolution at 40% contrast
Probe	7.636 lp/mm
Probe + image conduit	4.904 lp/mm
Probe + fiber optic	2.145 lp/mm

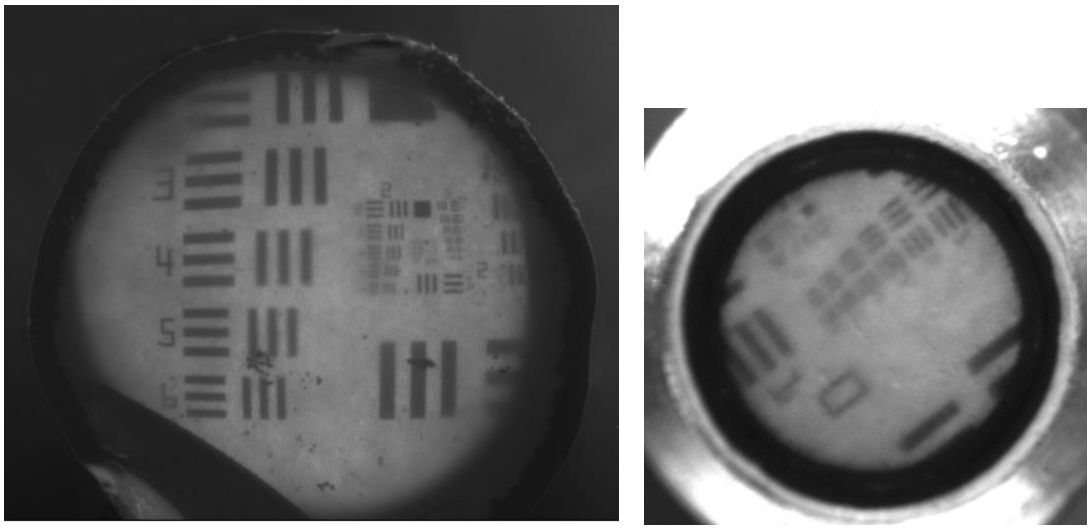

Figure 34. Test Target image using image conduit(left); and fiber-optic (right).

Since the image plane diameter is about 2.8 mm and the diameter of the image carrying fiber bundle is around 1.85 mm, there is a loss of information from the image boundaries. However, this might be advantageous, since the image boundaries were seen to have a high amount of distortion.

2.5 Using a High-speed Camera

Since PointGrey can be used at a maximum speed of 18 frames per second (18 fps), the frame rate might not be sufficient for high-speed applications, such as engine diagnostics or fireball studies. Thus, the MTF for the optical system using a FastCam SA-Z camera was determined. FastCam has a resolution of 1024 X 1024 pixels with a pixel size of 20μm X 20μm at 20,000 fps. It can be operated at 2100000fps. Since the image plane has a diameter of 2.8 mm the InfiniMax Microscopic lens was attached to the camera for magnification purposes. The air force test target was imaged using this setup to calculate the MTF. The optical system was found to have a resolution of 3.818 lp/mm at 30% contrast. This reduction was attributed to the small image size obtained on the camera (Refer to Figure 36). When the image was extracted the high magnification leads to a loss in clarity and contrast. This was due to the fact that the FastCam has a much larger chip size.

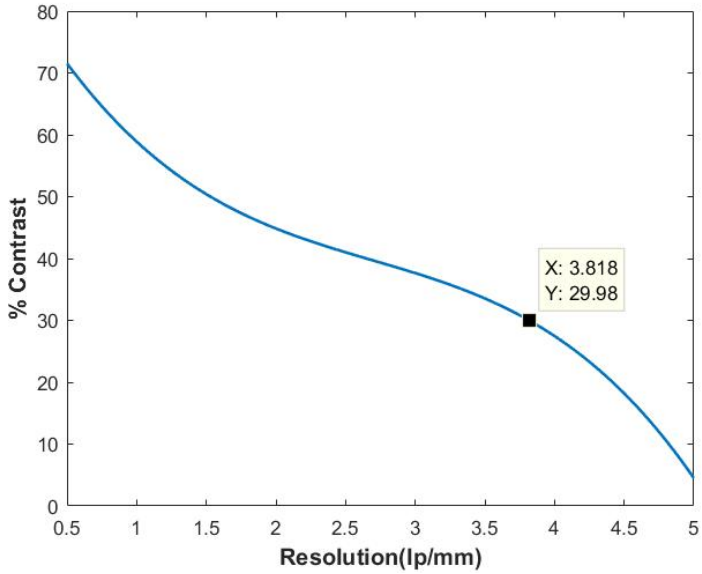

Figure 35. MTF plot for the optical system with FastCam SA-Z.

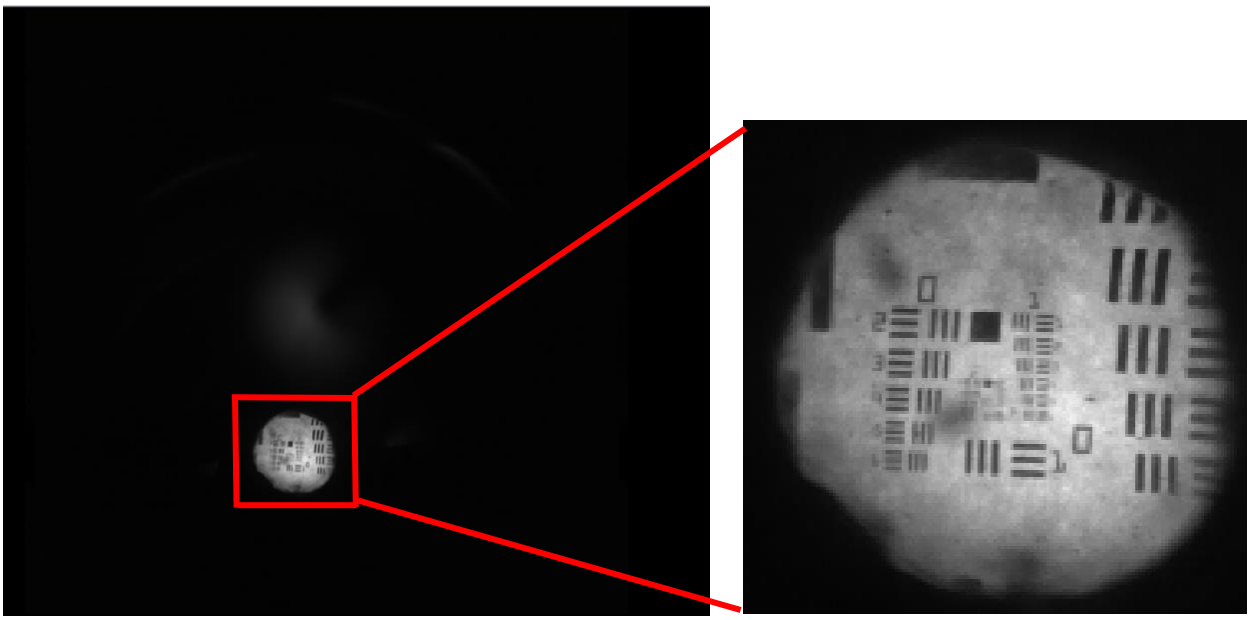

(a) (b)

Figure 36. Air force target imaged on FastCam SAZ at (a) 85% zoom; (b) 330% zoom.

2.6 Fireball Testing

Due to certain shortcomings, the testing of the probe on an actual engine was not possible. The explosion of gunpowder was recorded using the probe and image conduit to simulate the

combustion process in an engine. The probe was placed 50 mm away from the object. However, due to the limited field of view of 43°, the combustion process developed outside the probe boundaries. Figure 37 shows the progression of the combustion process imaged from the probe and image conduit assembly. This can be a potential problem while imaging combustion in IC engines.

Due to the high spectral intensity of the combustion process, no intensifier was necessary. Also, the camera chip size is 7.5 times the image conduit size. It was observed that on magnification, the images did not lose contrast due to the high intensity of the combustion process. Since the optical probe can be completely built using commercially available materials with good repeatability, the probe design can prove to be a very good option for use in explosive testing environments so as to avoid any damage to the camera. The use of fiber optics will make it possible to transfer the image from the optical probe image plane to a camera placed far away from the test setup. Fiber optics as long as 5-6 feet are available.

Similarly, the probe and imaging fiber assembly can be used for Tomographic-PIV experiments. Multiple probes can be used to image a fluid flow or flame simultaneously from different viewing angles. Imaging fibers will help transfer all the images to a common camera. These images can then be used to reconstruct the flow or flame in 3D to help determine various parameters of the flow as well as a three-dimensional velocity field in the case of PIV experiments.

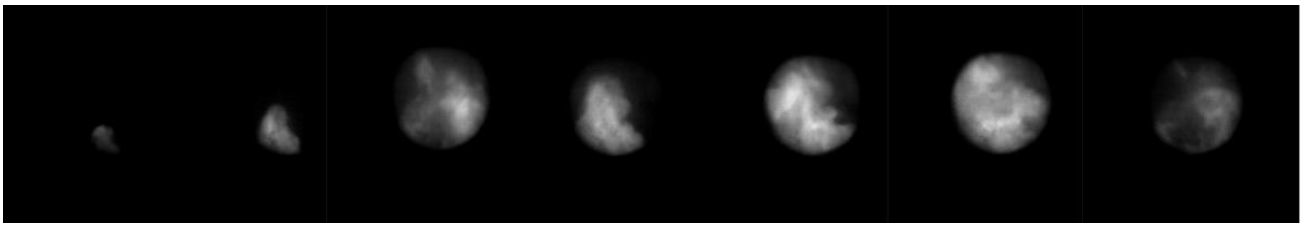

Figure 37. Fireball testing.

3. THREE-DIMENSIONAL RECONSTRUCTIONS USING THE PROBE

3.1 Background

3.1.1 Particle Image Velocimetry (PIV)

Velocity measurement depends on two factors: distance and time. Measuring the velocity of a solid object is easy since its displacement over time can be easily measured. Since gases and pure liquids do not have moving objects, measurement of flow velocity is difficult. A number of indirect measurement techniques, which make use of the well-established laws of physics have been developed. Some of these include the use of pressure probes, wind anemometers, etc. However, these are intrusive objects which can alter the actual fluid flow. Also, they provide readings at a single location. To measure the velocity field these objects, need to be moved in the direction of flow. As this process is not instantaneous only time-averaged data can be obtained. To overcome these limitations a number of optical methods have been developed. One of these methods is Particle Image Velocimetry (PIV). [25]

PIV is used to determine the instantaneous planar velocity field of flow. The experimental setup of a typical PIV experiment is shown in figure 38. As shown in the figure, the flow is seeded with tracer particles. The particles are introduced in the flow at a location where they will not affect the normal flow parameters. These particles are illuminated by a light source, usually a pulsed laser. The light scattered by the particles is recorded using a high-speed camera. The particles are illuminated twice over a certain time interval chosen depending on the flow velocity and magnification of the imaging system used. It is assumed that the particles follow the natural course of flow in this time duration. The local displacement vector is calculated for the two illuminations. Calibration is required to develop a relationship between the particle displacement in the image and that in the flow field. Once the calibration is applied, a 2-dimensional velocity vector over the time interval Δt can be obtained by comparing the two displacement vectors [25].

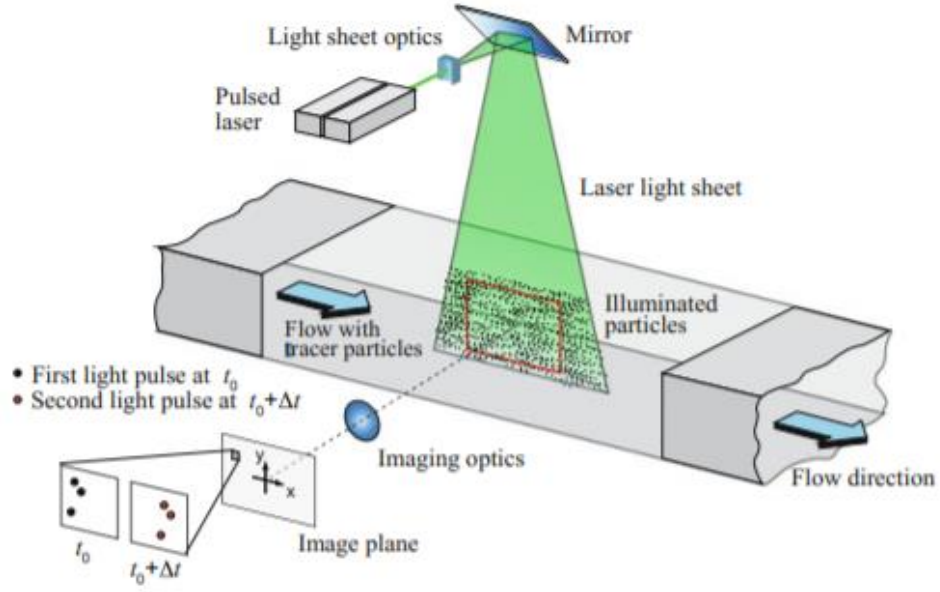

Figure 38. Experimental setup of a PIV experiment. [25]

The same principle can be extended to determine the velocity field in 3-dimensions for a complex unsteady and turbulent flow. One of the methods available to obtain the measurement of the velocity field in three-dimensions is 'Tomographic PIV'.

3.1.2 Tomographic Particle Image Velocimetry (Tomo-PIV)

Similar to the planar approach, images of illuminated tracer particles are obtained over a known time interval. However, instead of illuminating a planar region a three-dimensional volume is illuminated. Multiple cameras are used to view this illuminated volume. The data obtained from these cameras at a single instant is used to reconstruct a 3D image of the flow. Multiple reconstructions are generated from the obtained images over known time intervals. A cross-correlation of these reconstructions helps develop a three-dimensional velocity field. Figure 39 provides a schematic illustration of the tomographic PIV technique. The following sections discuss provide information about the various parameters that affect Tomo-PIV quality.

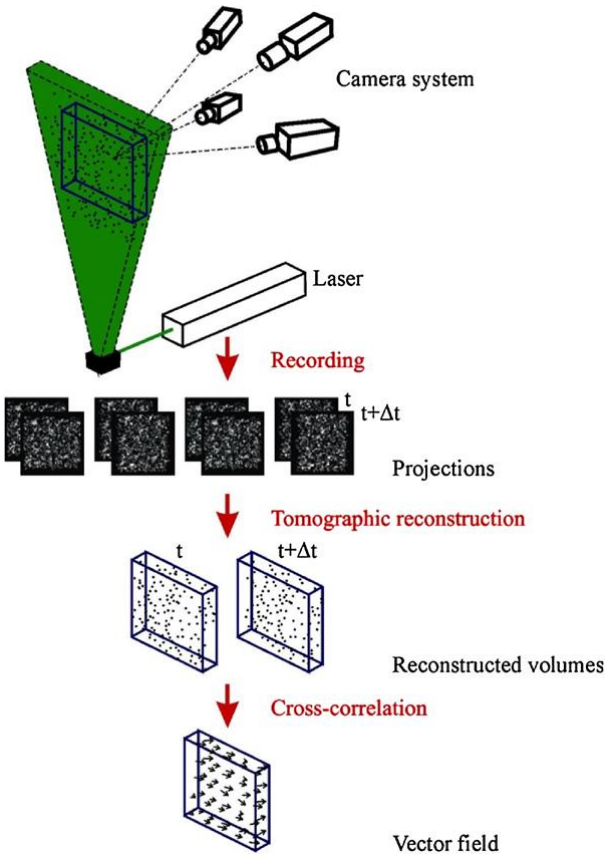

Figure 39: Schematic illustration of Tomographic PIV technique [25,26].

3.1.2.1 Volume Illumination

Typically, a laser system is used to illuminate a volume of flow. As compared to planar-PIV, obtaining a volumetric illumination requires a simpler optical design. Since most of the Nd: YAG lasers have an exit diameter of 1mm, it is possible to obtain volumetric illumination using a single cylindrical diverging lens.

Spreading of light over a larger area may lead to reduced intensity. Certain modifications may be necessary to improve the intensity of illumination. A double pass filter was suggested by Scarano et al [27]. This includes the use of a reflective plane mirror on the opposite side of the flow normal to the axis of the laser beam. The mirror will reflect the light back onto the region of interest so that it is illuminated a second time.

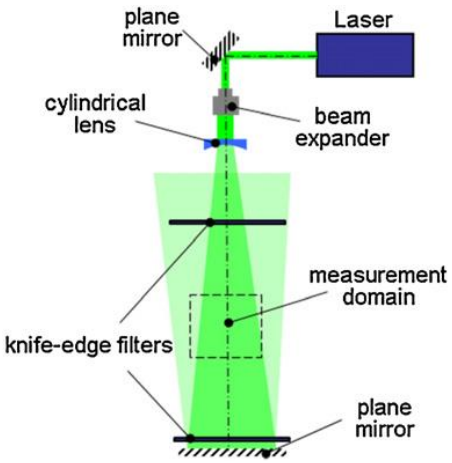

Figure 40: Schematic illustration of the double-pass technique [27].

Knife-edge filters are used to restrict the light intensity to the required measurement volume. Using the double-pass technique will ensure that all the cameras receive forward scattered light directly from either of the two passes.

3.1.2.2 Viewing angles and angular aperture

The accuracy of tomographic PIV is based on the quality of the 3D reconstruction of the flow field. It is highly important to ensure that the imaging systems chosen are such that all the particles in the illuminated volume are in focus. Also, the number of cameras used to capture the images and the angles at which the cameras are oriented plays an important role in determining the quality of the reconstructions. It has been seen that two cameras are insufficient to produce an accurate reconstruction of the 3D object. Adding more cameras improves the quality of the reconstructions since more information about the object is available. However, it is seen that the quality factor approaches unity when 5 cameras are used. The quality factor is obtained by comparing the exact and reconstructed intensity distributions. [28]

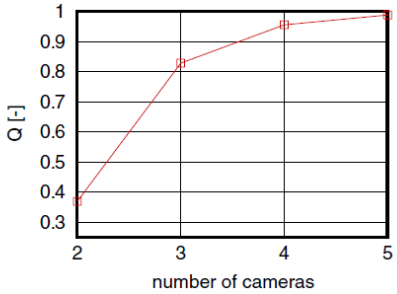

Figure 41. Variation in reconstruction quality as a function of the number of cameras [26].

The cameras can be placed either in a linear arrangement or a cross arrangement, as shown in Figure 42. Another factor influencing the reconstruction quality is the value of the angle between the lines-of-sight of the two farthest cameras in the configuration. This is denoted by β (Refer to Figure 42). The spatial resolution of the object depends on the maximum value of the angular aperture. Elsinga et al. [26] have reported that the quality of reconstruction is maximized when the value of β lies between 40° and 80°. However, further increase leads to reduced quality. This can be attributed to the fact that larger angular separation leads to longer intersection of the lines-of-sight in the measurement volume leading to increased particle density. Also, smaller angles lead to the formation of elongated particles along the Z direction (depth). Figure 43 shows the effect of the value of β on the reconstructions.

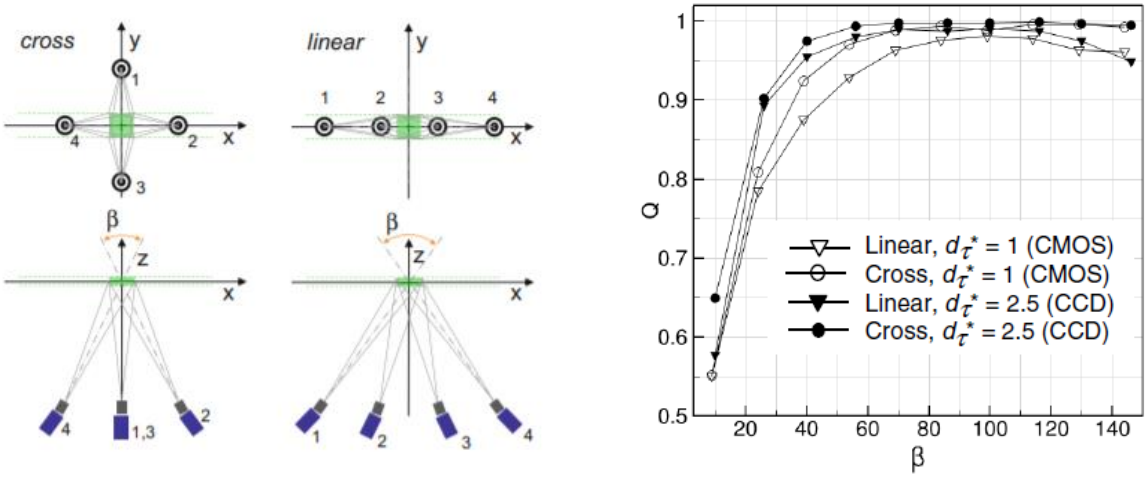

Figure 42. Orientation of the cameras (left); variation in the quality factor as a function of the viewing angle (right) [25,28].

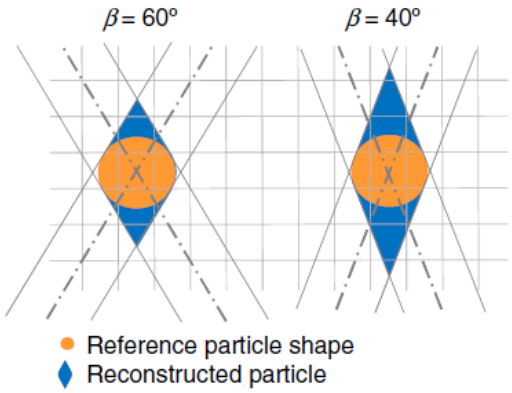

Figure 43. Effect of angular aperture on the reconstruction [25,28].

Also, the cameras should not be collinear with each other. This is only possible when the two viewing angles are placed 180° apart, i.e. the cameras are opposite each other. Usually, a variation of one degree between the cameras is enough to ensure a non-collinear arrangement. [25,26,28]

3.1.2.3 Seeding Density

High seeding density is not desirable for Tomo-PIV because tracking the motion of individual particles becomes difficult. Also, it might result in scattering of light leading to poor image contrast. Thus, a seeding density of 0.05 particles per pixel (ppp) was suggested for a 4 camera configuration. A higher seeding density is suitable for a system with a higher number of cameras (around 0.2 ppp was used by Lynch et al [29]). Conversely, levels of ppp between 0.005 and 0.022 are considered inadequate for a good reconstruction [25].

3.1.2.4 System calibration

The most important aspect of any tomo-PIV experiment is the reconstruction of the flow field. A good reconstruction will lead to a better estimation of the velocity flow field.
The first step in the reconstruction process is system calibration. Consider that the physical space is defined by (X, Y, Z) and its projection in the image space is represented by (x_i, y_i) and M is the mapping function.

$$(x_i, y_i) = M_i(X, Y, Z) \quad (1)$$

The reconstruction quality depends on the correct determination of the mapping function. Either a third-order polynomial or pin-hole model is used for the determination of the mapping function. The calibration process helps identify the position and magnification of various points on the image plane with respect to the different viewing angles. It is important to ensure that the lines-of-sight from various viewing angles intersect precisely to get a good quality reconstruction.

3.1.3 Reconstruction Algorithm

The 3D intensity distribution can be represented as an array of voxels which results in an intensity $E(X, Y, Z)$ corresponding to the physical space (X, Y, Z). Three-dimensional space is

divided into a number of evenly spaced rows and columns. Each 3D cube is called a voxel and has a color intensity associated with it. A pixel can thus be considered equivalent to one pixel in 2D. For tomographic reconstructions, voxels are considered spherical [31]. Projection of the volume intensity at the i^{th} pixel position of the image (x_i, y_i) gives the pixel intensity $I(x_i, y_i)$ [25]. The relation between these two can be written as:

$$\sum_{j \epsilon N_i} w_{i.j}\, E(X_j, Y_j, Z_j) = I(x_i, y_i) \qquad (2)$$

where N_i denotes the number of voxels contributing to the image intensity at the i^{th}pixel and $w_{i.j}$ is a weighting factor that measures the contribution of each voxel to the pixel intensity. Figure 44 represents the reconstruction model that is generally used. The imaging plane is represented as a line of pixels and the voxels are represented as a plane of spheres. The value of the weighting function for a particular voxel depends on the volume overlap between the line of sight and the chosen voxel. The shaded voxels are the ones that have a non-zero value for the weighting coefficient. The difference in shading represents the reducing value of the weighing function from the center to the sides. A solution of equation (2) is the basis of the reconstruction algorithms used in tomo-PIV. A number of algorithms have been developed to solve the equation. Multiplicative algorithmic reconstruction technique (MART) is the most popular amongst them and has been used for reconstructions in this work. MART is based on the line-of-sight principle. The image intensity along the available viewing angles is smeared through the measurement volume. The point where the lines-of-sight coincide, a 3D geometry is reconstructed. This guessed geometry is then used to obtain projections along the various viewing angles. The guessed projections are compared with the available image intensity. Depending on the differences between the two, the voxel intensity is varied. This process is repeated depending on the number of iterations specified by the user. [38]

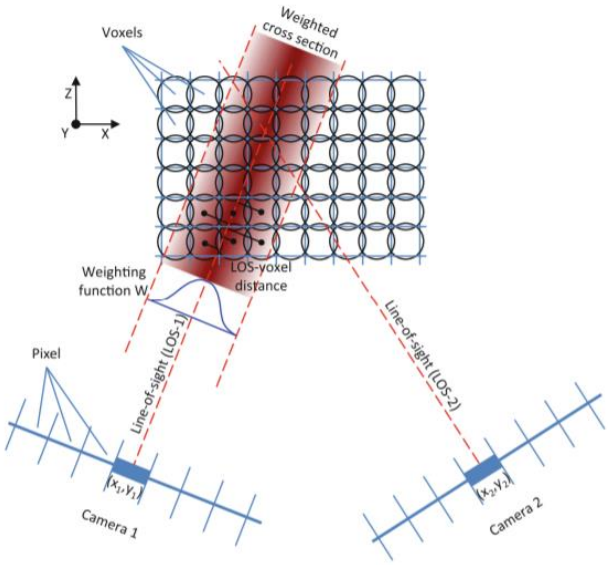

Figure 44. Representation of the reconstruction model for Tomo-PIV [31].

3.1.4 Experimental setups for Tomography based experiments

Meyer et al. [39] have demonstrated the use of multiple cameras to detect the spatial and temporal distribution of soot in a turbulent flame using laser-induced incandescence. The process involved the use of lasers to heat the soot particles near or above their sublimation temperature. The fluorescence from heated soot particles was then detected using multiple high-speed cameras. The signal from different cameras was then used to develop a 3D distribution of soot particles. Figure 45 shows the setup used. It was observed that four cameras were sufficient to obtain good results.

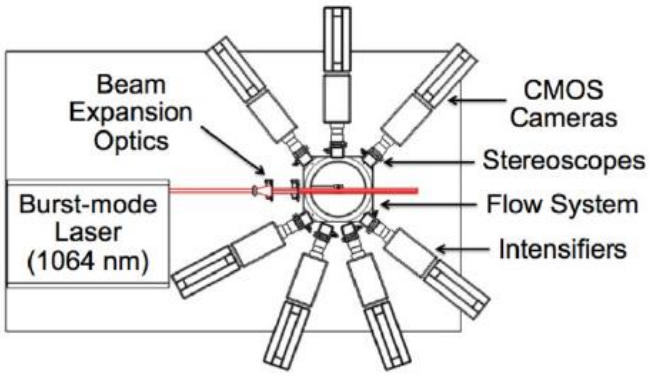

Figure 45. Experimental setup for laser-induced incandescence of soot particles [39].

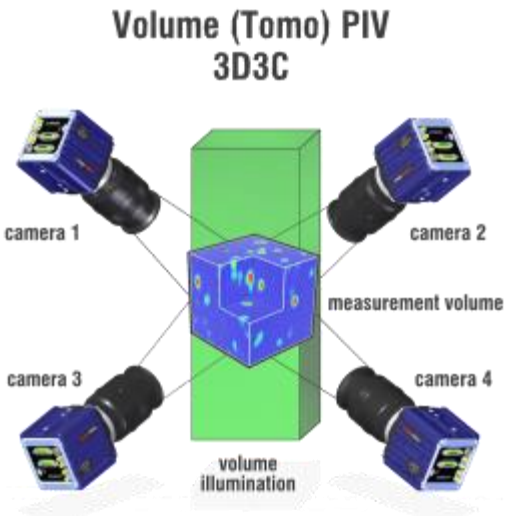

Figure 46. Tomographic PIV experiment using four cameras [32].

A similar multi-camera setup is used for Tomo-PIV experiments. As shown in figure 46, four different cameras are positioned so as to get different views of the object. All four cameras have to be placed at the exact same distance from the object. Also, all of them need to be triggered at the same time so as to get instantaneous measurements, thus increasing the complexity of the system. Such a system also takes up a lot of space.

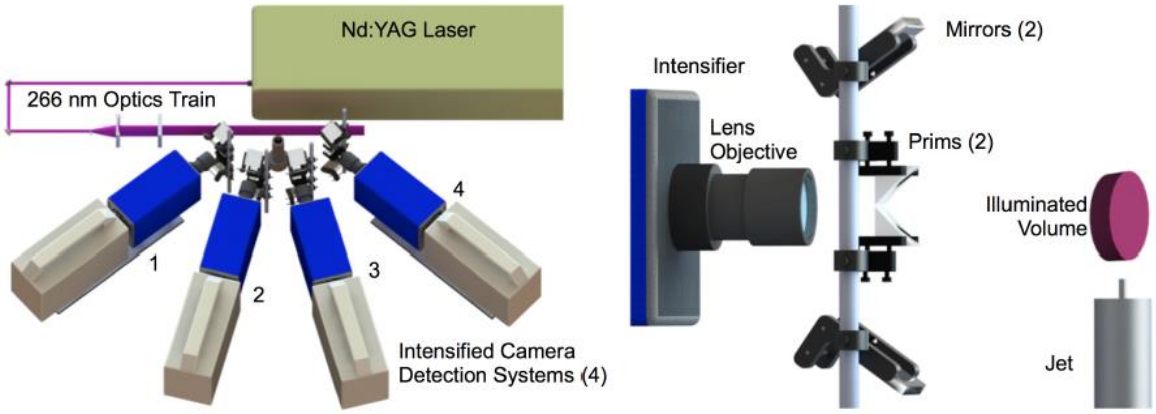

Figure 47. Experimental setup with cameras and stereoscopes (left); a detailed view of stereoscope arrangement (right) [40]

Figure 47 shows the development of a stereoscope to capture two views using a single camera. Four such cameras were used to obtain 8 views of the object by Halls et al. [40] for laser-induced fluorescence imaging in a jet flow. The software used for reconstructions, DaVis 8.0, limits the number of views that can be used to eight. Thus, four cameras are used. The need to couple more

viewing angles on one camera was identified. Thus, a quadscope arrangement was developed to image 4 angles on a single camera [41]. A quadscope consists of four prisms and four mirrors used to obtain four different views of the object (Refer to Figure 48). In spite of using one camera to obtain all the images, the quadscope was found to have the following shortcomings:

- The flow can be imaged only from one side
- The quadscope needs to be placed within the focal length of the camera thus placing certain restrictions on the design of the experimental setup.
- Only four views of the object/flow are obtained with little variation in the viewing angles used

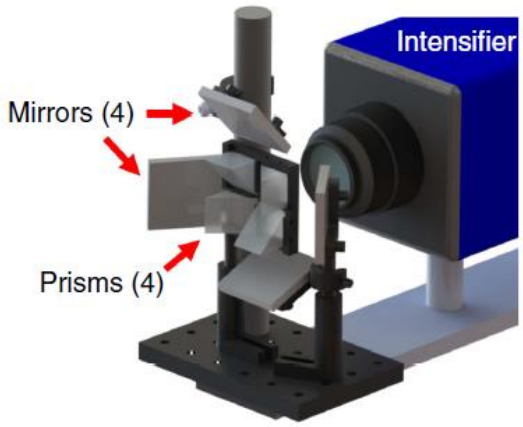

Figure 48. Schematic of quadscope [41]

To overcome the above limitations, the possibility of using the optical probe and fiber optic assembly for 3D reconstruction experiments was explored. The optical probe assembly was found to have the following advantages over the quadscope:

- One of the main requirements for Tomo PIV experiments is to have a good depth of view so that all the particles within the volume of interest are in focus. As discussed in section 2.3.2 the optical probe was practically seen to have a depth of view of 120 mm.
- Optical fibers are used to transmit the image from the image plane of the probe to a high-speed camera. Optical fibers as long as 5 feet are available. Thus, the probes can be located close to the object with the camera located far away.
- Since the probe is assembled within a half-inch diameter, 3-inch long lens tube, it was found to be very handy and could be positioned on either side of the object.
- There is no restriction on the number of probes and the angles at which they can be oriented. Thus, an object can be visualized in as many directions as necessary.

Due to the following advantages, the probe and fiber optic assembly was considered to be a good alternative to the use of quadscope for 3D reconstruction and Tomo PIV experiments

especially for applications involving explosive material. The probe was found to be comparatively cheap to build due to which any damage to the probe was better than damage to the camera.

Thus, to test the possibility of using the probe for tomo-PIV applications in the future, a sewing pin with a spherical head was imaged and reconstructed using the probe assembly. The quality of the reconstructions obtained was assessed to determine the optimum design for a Tomo-PIV experiment using multiple probes and imaging fibers.

3.2 Experimental Setup

Since the pin is symmetric around the Z-axis and has known dimensions and shape, it was considered to be suitable for calibration and testing of the probe. The pin is also small in size and has a fairly consistent light intensity. Since the reconstruction quality depends on the distribution of light intensity, the pin is a suitable object for checking the quality of the reconstructions.

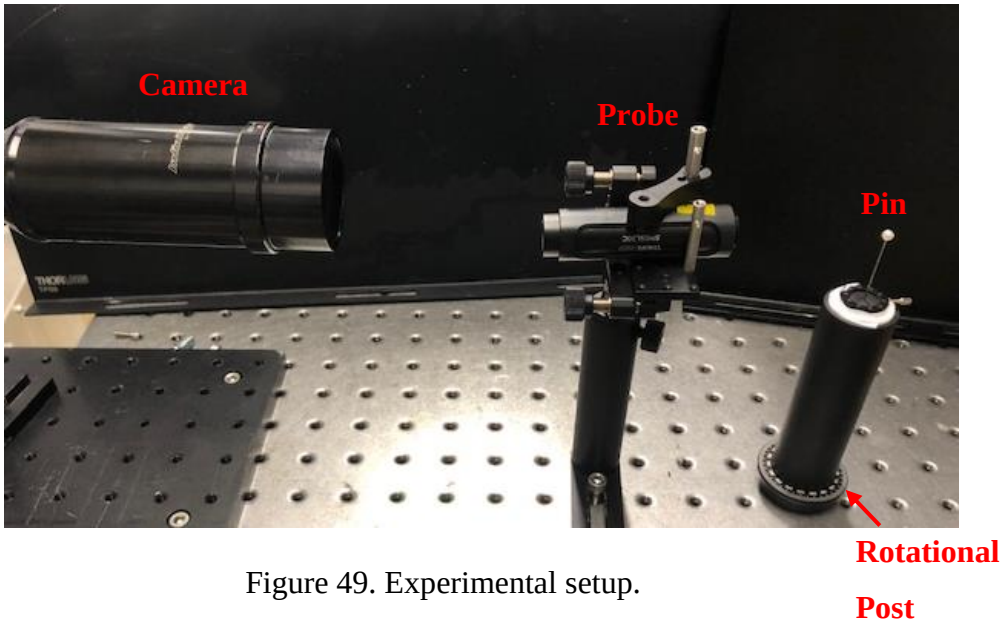

Figure 49. Experimental setup.

Figure 49 shows the experimental setup used. Since a single fiber and probe were available, the object was placed on a rotary mount and rotated in intervals of 5 to 15 degrees. Since the object imaged was solid, imaging the object by rotating it can be considered to be equivalent to taking images using multiple probes at different viewing angles. Images of the object and a calibration plate were taken after each rotation. It is important to ensure that the calibration plate was placed at the same location as the object. Once the images were recorded, the reconstructions were done on DaVis, an image processing software provided by LaVision, specifically for PIV applications.

Figure 50 shows the calibration plate used. It is compatible with DaVis and has two planes marked with dots of known dimensions. PointGrey camera with InfiniMax microscopic lens was used for imaging. The step-by-step procedure for the reconstruction of a pin with 4 views is discussed below:

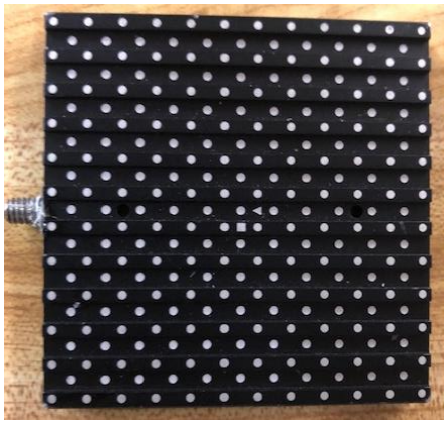

Figure 50. Calibration Plate.

Step 1: Acquiring object and test target images

Care was taken to ensure that the distance and orientation of the calibration target were the same as that of the object. Also, the magnification was kept constant while taking images of the object and the calibration plate. The illumination need not be the same for object and calibration target but it should be constant and uniform while taking pictures of the object. Since the reconstructions were based on the distribution of light intensity in the captured image, it was necessary to maintain a good contrast between the object and its background. Thus, a white pin was imaged on a black background. Figure 51 shows the raw images of the object and the calibration test target acquired on the camera.

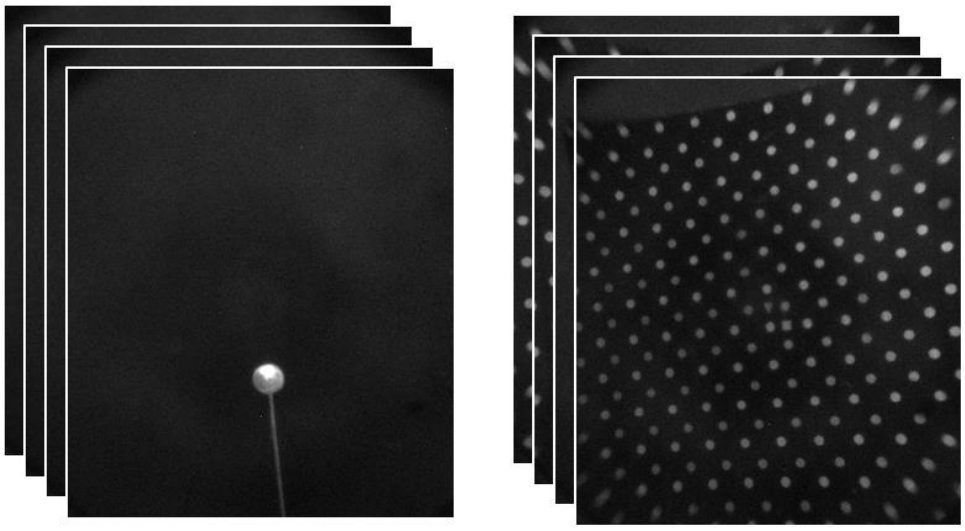

Figure 51. Object(left); and test target (right) imaged at 30°, 15°, -15° and -30°.

Step 2: Importing the images on DaVis

The object and calibration plate images should have the same size.

Step 3: Calibration

The calibration plate images were used to identify object inclination with respect to the line of sight. The software then calibrated and reconstructed the calibration plate according to the angles it perceived. The angles identified by the software were: 33°, 16.8°, -10.1° and -26.2°. Figure 52 describes the calibration process. Although the angles were not identified exactly, since the object and the calibration plate were imaged at the same orientation and at the same distance from the optical probe, the error in angular positioning does not have any effect on the reconstruction of the object. The mapping function used to calibrate the system corrects image distortion. Once the calibration process was completed the object images were scaled according to the calibration.

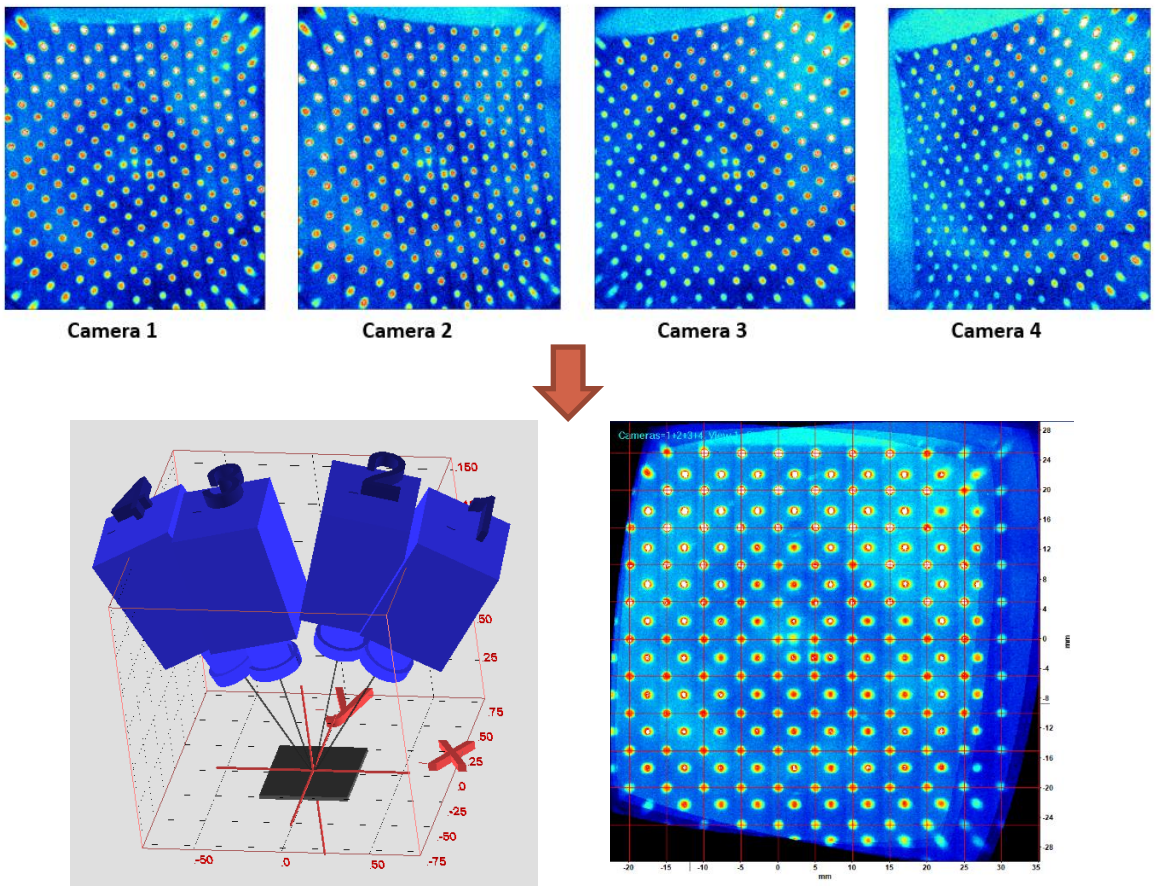

Figure 52. Calibration plate images for the 4 views(top); Position of the cameras identified on DaVis (Bottom left); Reconstructed calibration plate (bottom right).

Step 4: Processing the object images

After pre-processing the images to ensure smoothness, good contrast, and less noise, three-dimensional reconstructions were carried out based on the MART algorithm.

Figure 53 shows the projected volumes of the reconstruction created.

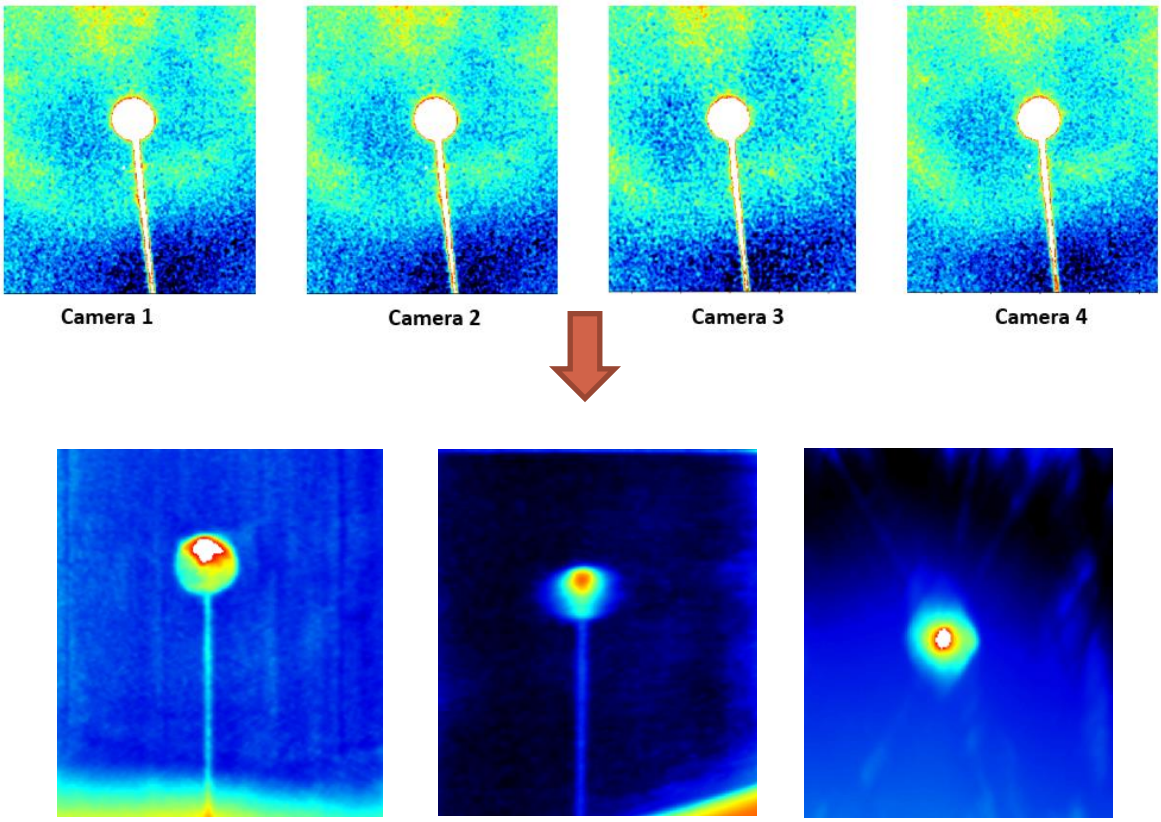

Figure 53. Object Images for the 4 views (top); Projected Volume in XY direction (bottom left); YZ direction (bottom center); XZ direction (bottom right).

Step 5: Using MATLAB

The reconstructions are in the form of stacks of images in the Z direction. Thus, MATLAB is used to condenses these images in a three-dimensional figure that can be analyzed using Tecplot.

Step 6: Visualizing the 3D structure on Tecplot

Tecplot is used to analyze the dimensions and quality of the reconstructed object. Figure 54 shows the final 3D reconstructed structure.

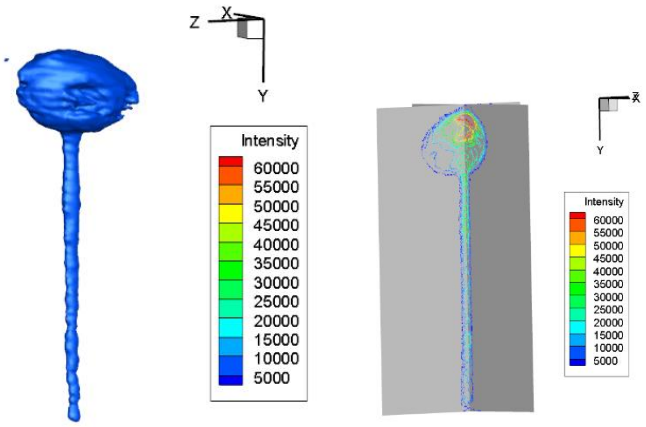

Figure 54. 3D reconstruction of pin using 4 views (left); Sliced view of the reconstruction (right).

The flowchart below briefly summarizes the steps involved in the reconstruction process:

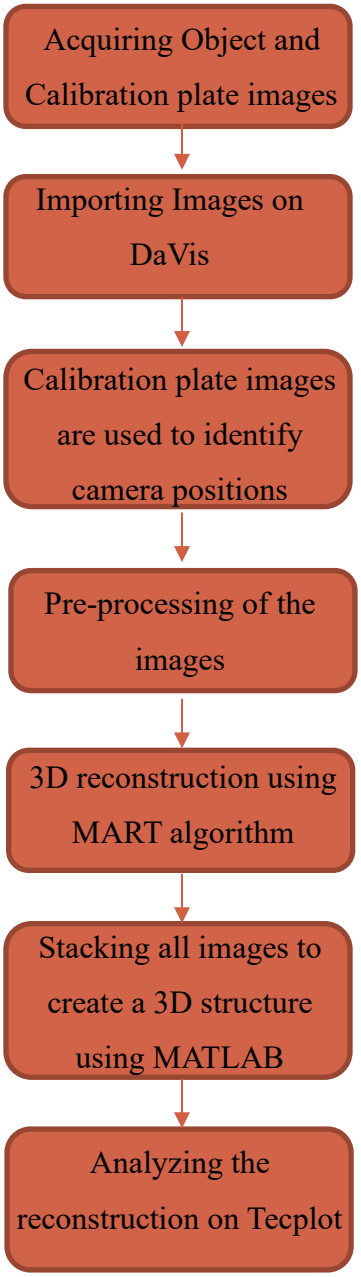

3.3 Analysis of the Reconstructions

To compare the quality of reconstructions, the pin was imaged directly through the probe and probe and imaging fiber.

The reconstructions were divided into following sub-groups:

1. Using Probe
    i) Number of views (2/3/4/5/6/7) – a maximum of 8 views can be calibrated on DaVis
    ii) Reconstructions with front angles and front and back angles
    iii) Number of iterations performed
2. Using probe and fiber optic

3.3.1 Reconstructions using Probe:

Reconstructions using 2 to 7 views were obtained to find the optimum number of views necessary to get a good quality reconstruction. The quality was measured by comparing the diameter of the reconstructed pin sphere with its original value. As discussed in section 3.1.2.2, the quality of reconstructions is the best when the angle between the farthest two views lies between 40° and 80° since it avoids long intersections of line-of-sight. Also, figure 55 shows that the image of the calibration plate when viewed at 60° from the normal. It was very difficult to distinguish between the two planes. This increased the error in calibration and inversely affected the reconstruction quality.

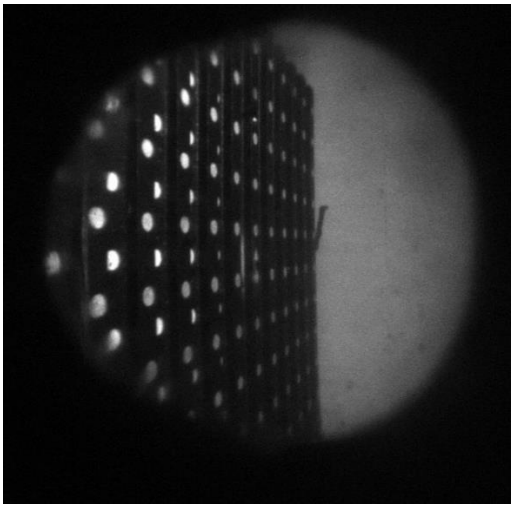

Figure 55. Image of the test target at 60°.

Conversely, a smaller angle between the line-of-sight leads to the formation of a longer particle along the Z-axis (depth). This can be clearly seen in the pin reconstruction with 2 angles (Refer figure 54). The angle between the line of sights was 35°. Thus, 0°, 15°, 30°, 35°, -15°, -30° and -35° were the angles used for reconstructions, keeping the maximum aperture angle less than 70°.

As the number of viewing angles were increased the elongations started reducing. Moreover, the error in the obtained sphere diameter reduced. There was a significant reduction in the error up to 5 angles beyond which the graph flattened (Figure 56). The viewing angles were restricted to a maximum of 70°.

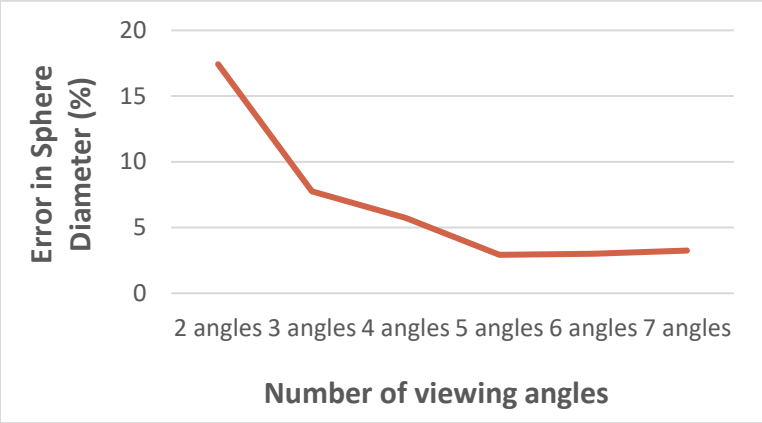

Figure 56. Plot of error in the reconstructed diameter against the number of viewing angles.

Table 11. Analysis of reconstructed object.

Number of viewing angles	Angles	Sphere diameter (mm)	Error (%)
2 angles	0-35	4.697	17.425
3 angles	30-0-330	4.31	7.75
4 angles	0-15-30-35	4.229	5.725
5 angles	330-345-0-15-30	4.117	2.925
6 angles	330-345-0-15-30-35	4.12	3
7 angles	325-330-345-0-15-30-35	4.13	3.25

2 Angles *(0°/35°)*

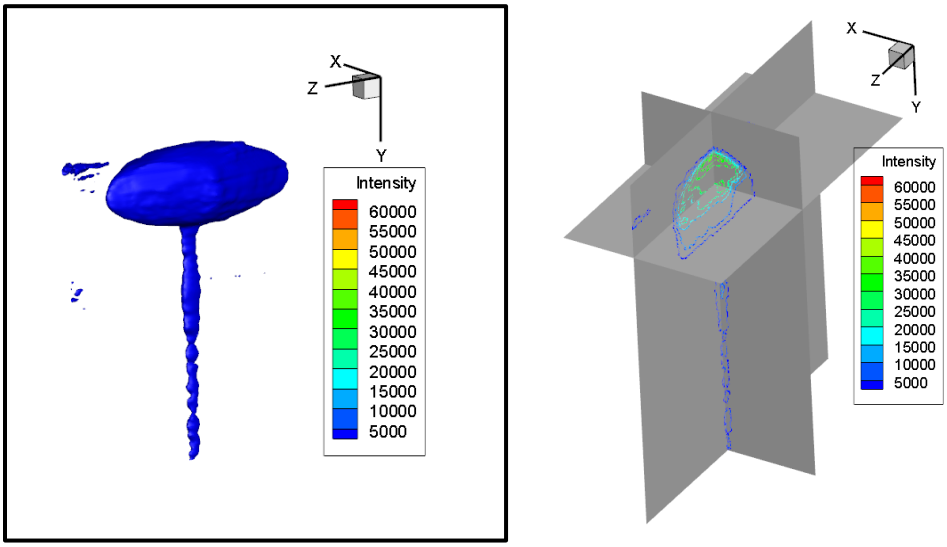

Z-Slice X-Slice Y-Slice

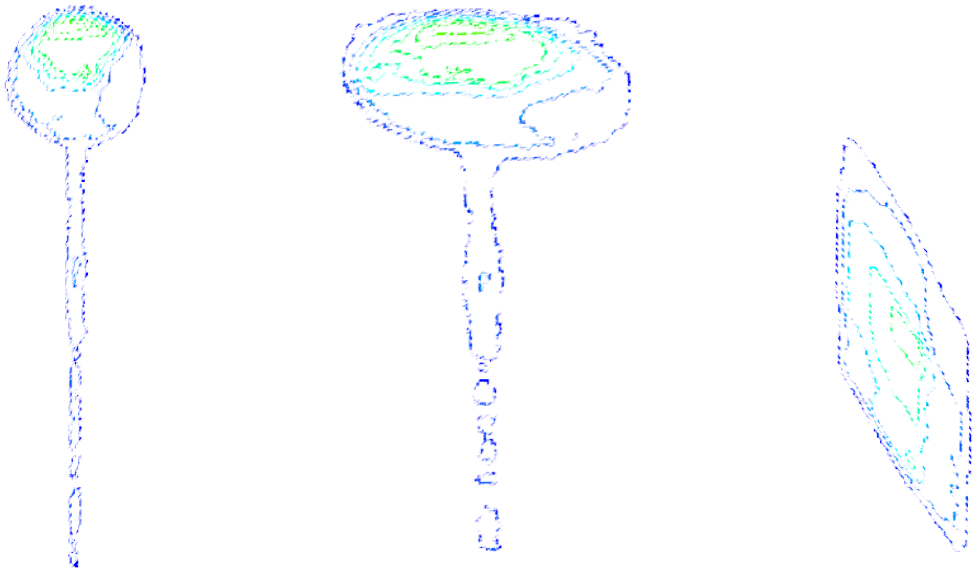

Figure 57. Different views for reconstructions using 2/3/4/5/6/7 viewing angles.

Figure 57 continued.

3 Angles (*-15°/0°/15°*)

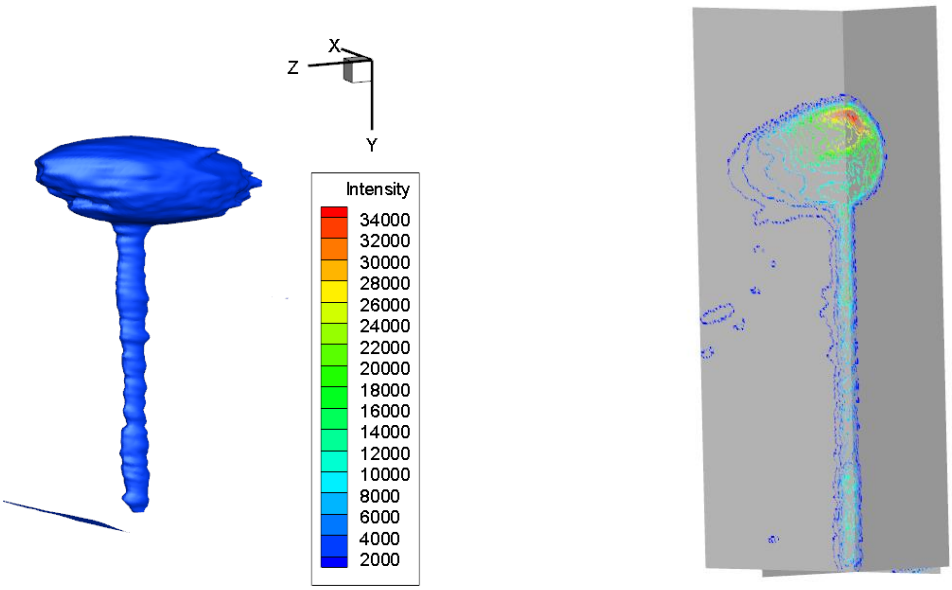

Z-Slice

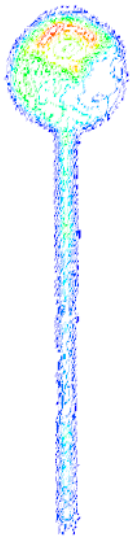

X-Slice

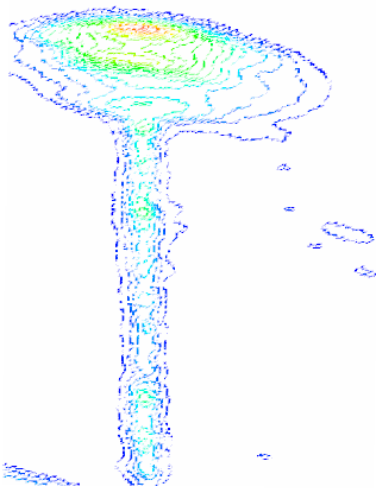

Y-Slice

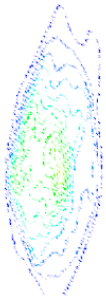

Figure 57 continued.

4 Angles (*-30°/-15°/15°/30°*)

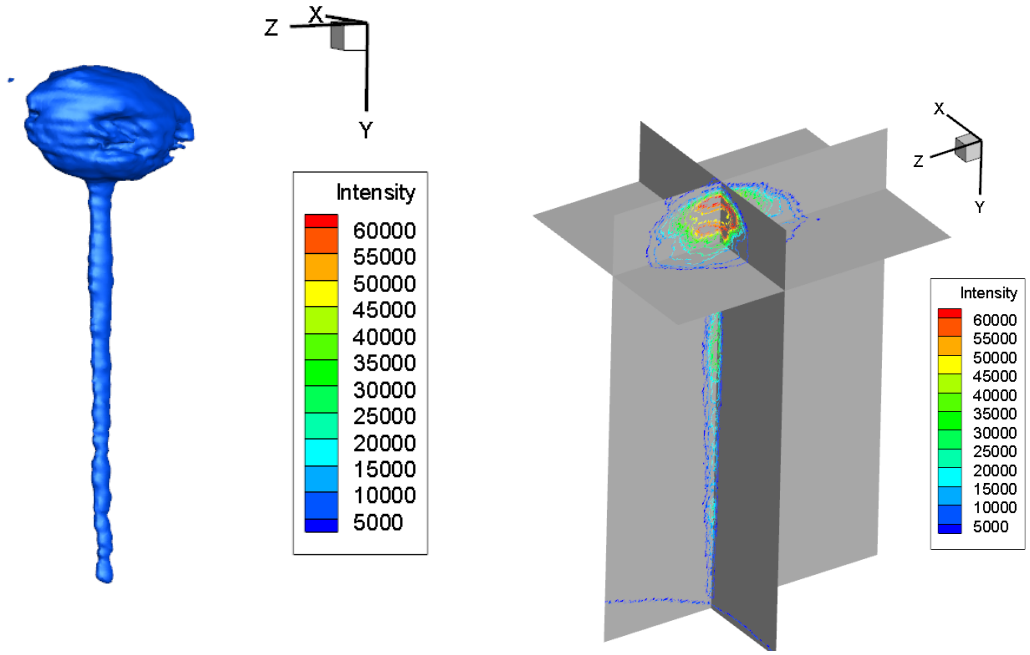

Z-Slice

X-Slice

Y-Slice

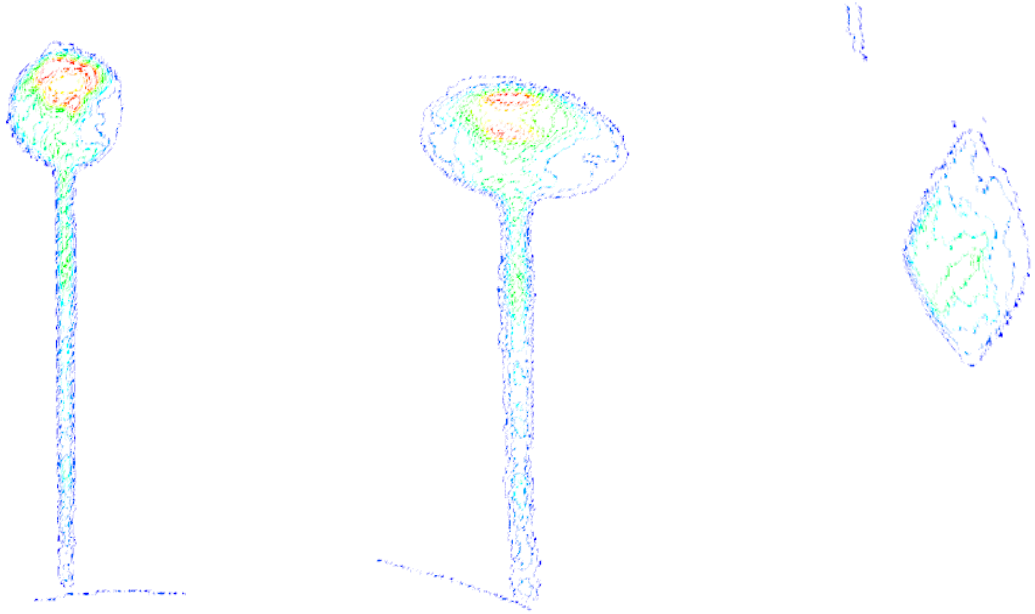

Figure 57 continued.

5 Angles (*-30°/-15°/0/15°/30°*)

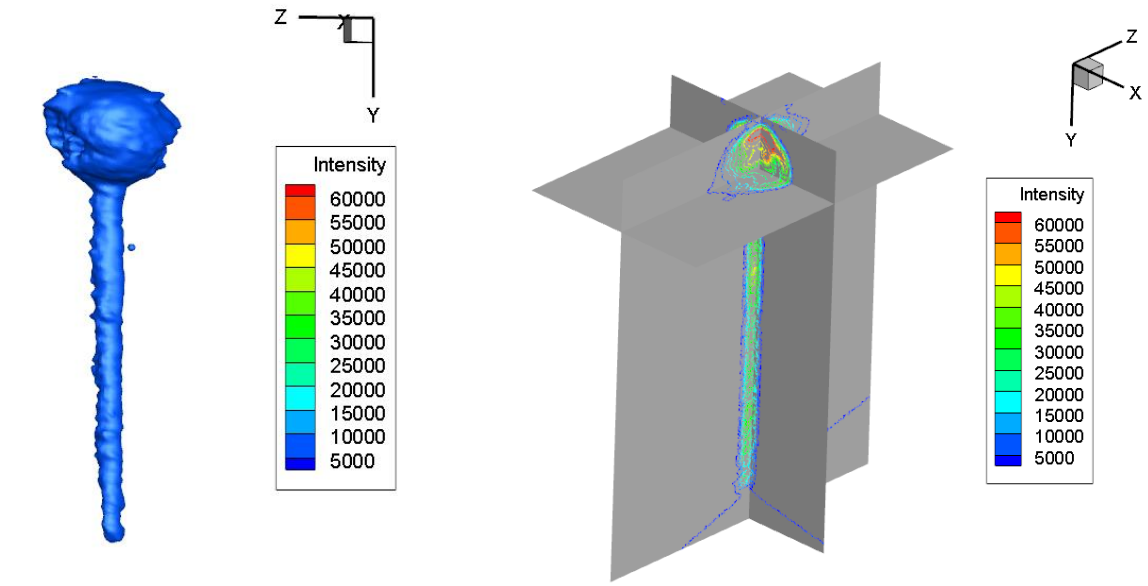

Z-Slice

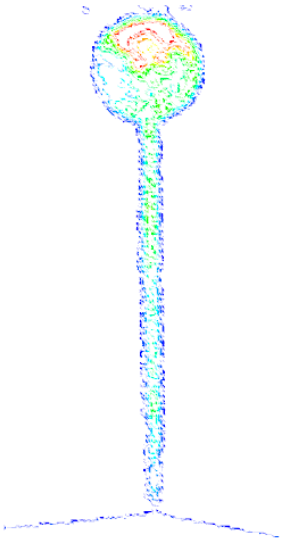

X-Slice

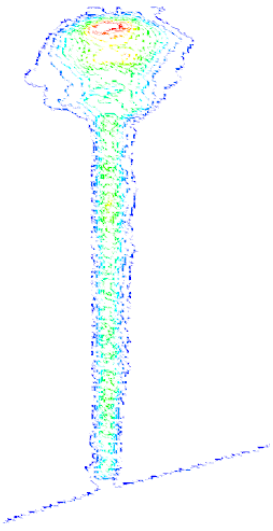

Y-Slice

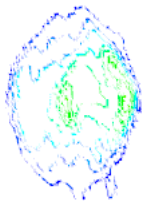

Figure 57 continued.

6 Angles (*-30°/-15°/0/15°/30°/35°*)

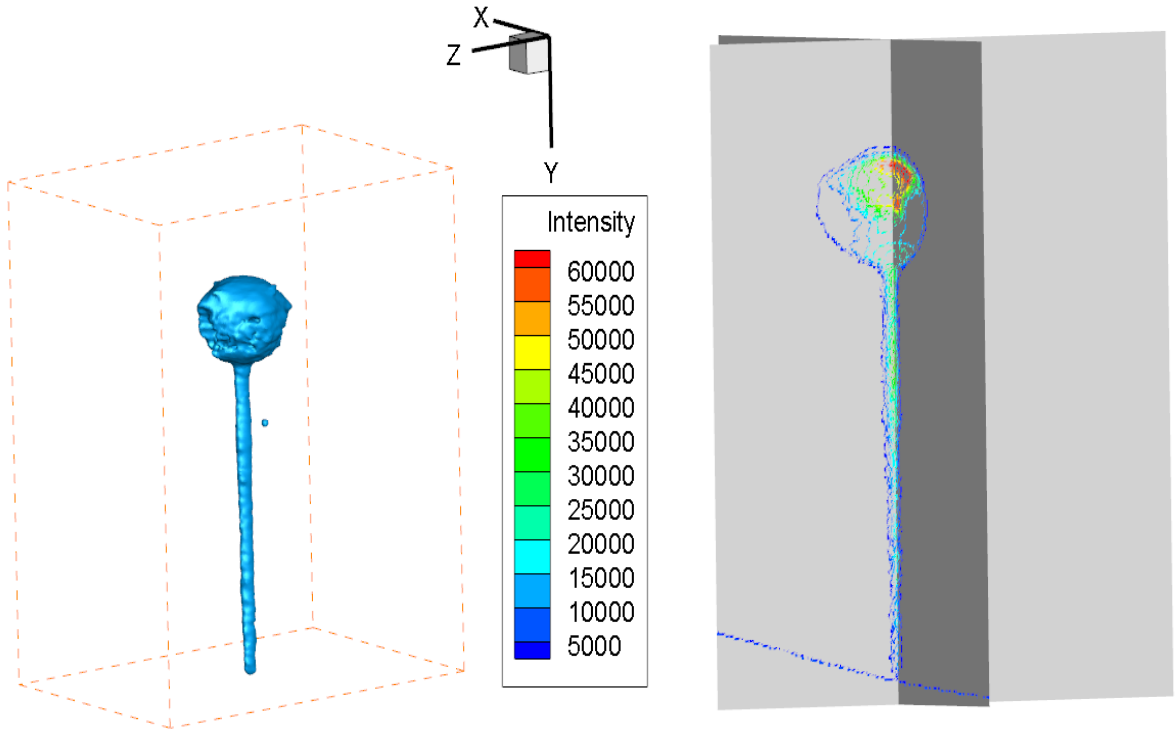

Z-Slice

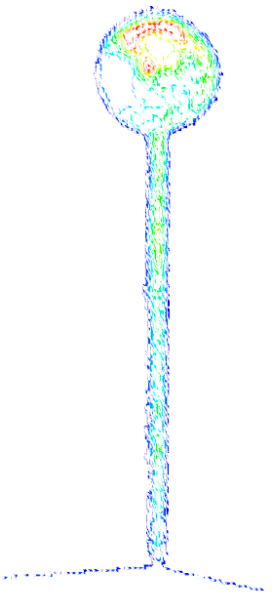

X-Slice

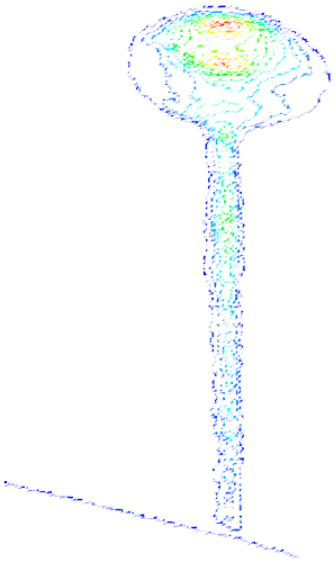

Y-Slice

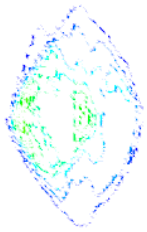

Figure 57 continued.

7 Angles (*-35°/-30°/-15°/0/15°/30°/35°*)

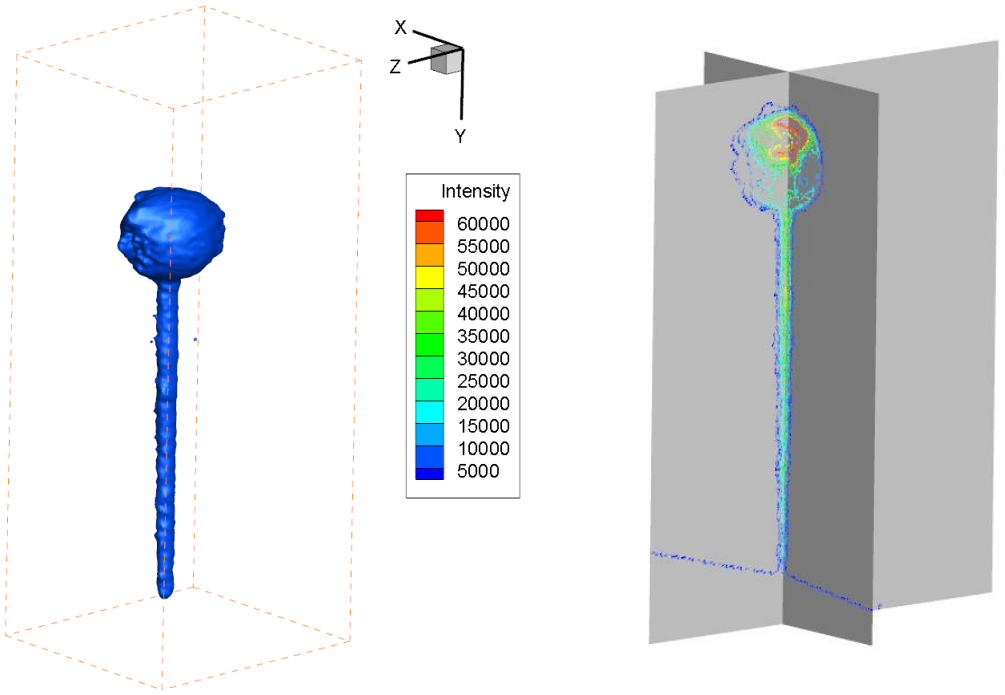

Z-Slice

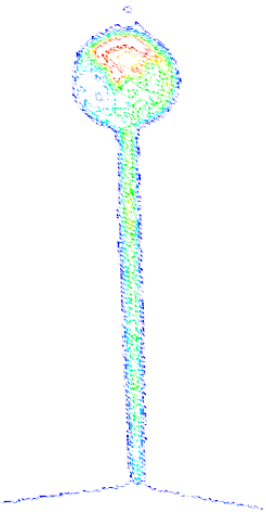

X-Slice

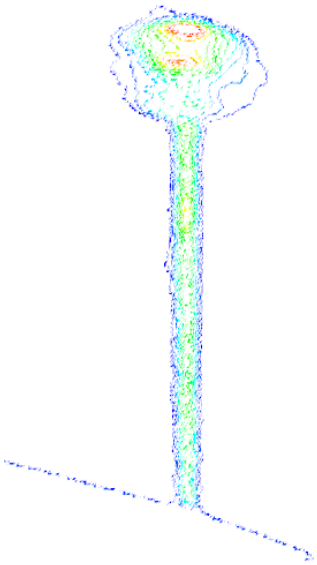

Y-Slice

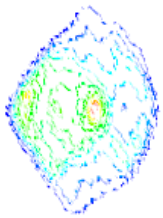

The next set of results was obtained by changing the number of iterations performed to get the reconstruction for the same set of viewing angles. The reconstructions were obtained for a set of 7 viewing angles. 3,5,8,15,30,50 and 100 iterations were run. Figure 58 shows the different views of the reconstruction for 3 iteration case. The XY plane shows an almost perfect spherical object, however there is significant stretching along the YZ plane. It was observed that as the number of iterations changed the elongation seen in the YZ plane kept reducing with no change in the XY plane. Figures 59 and 60 represent the changes in the sphere diameter with increasing iterations for YZ plane. There was significant reduction in the size up to 30 iterations beyond which the reconstruction remained almost same.

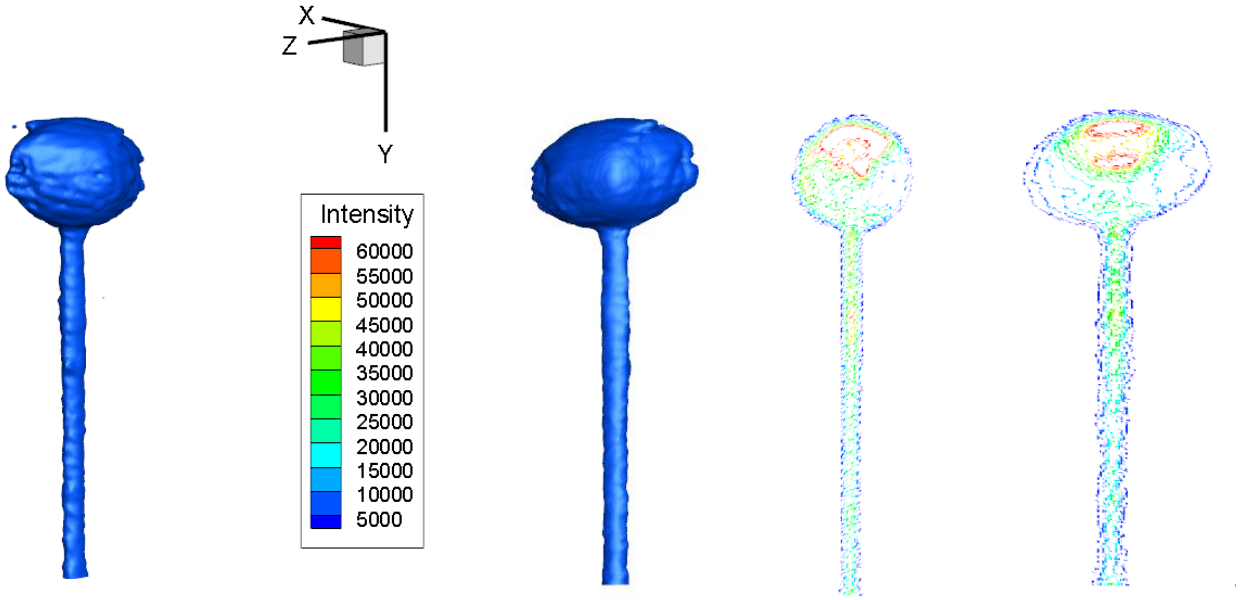

(a) 3D object

(b) YZ plane

(c) Z slice

(d) X slice

Figure 58. Different views for reconstruction with 3 iterations.

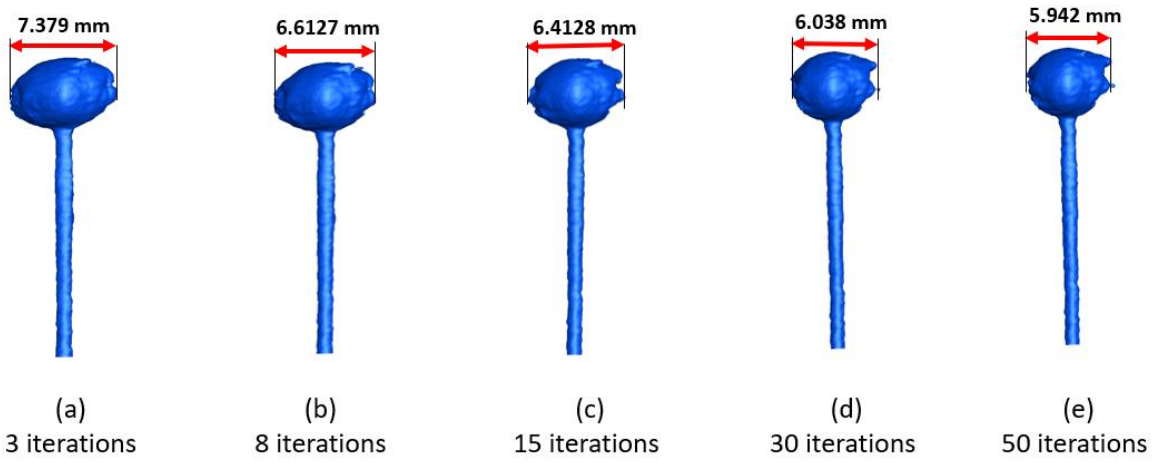

Figure 59. Changing sphere diameter along the YZ plane.

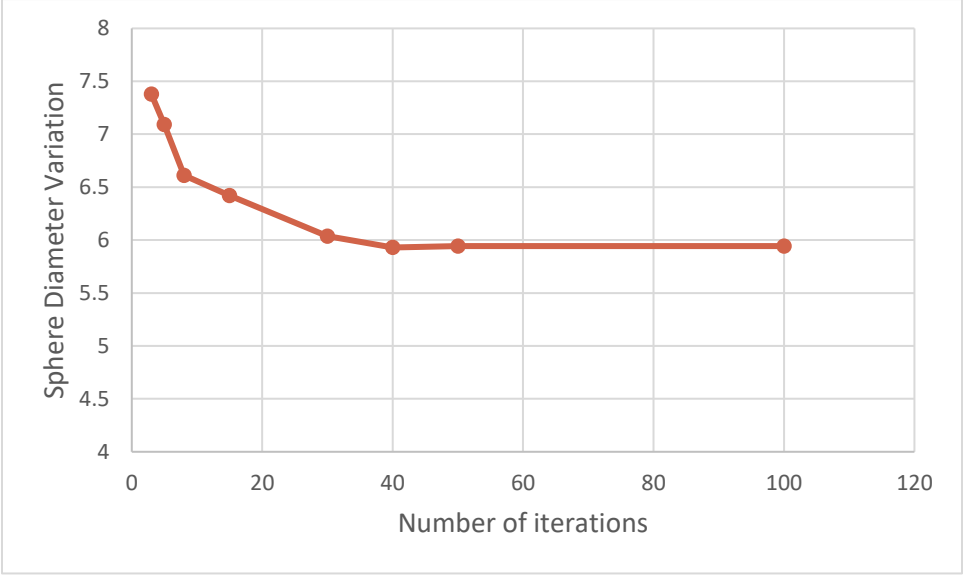

Figure 60. Variation in sphere diameter along the YZ plane with the number of iterations.

The procedure explained above is useful only for solid objects or objects with a constant geometry. For flows field or sprays, images need to be taken simultaneously from different viewing angles. This requires the use of multiple probes and imaging fibers so that images can be obtained simultaneously on the same camera. Since the same optical setup will be used for all viewing angles the resolution for all images will be the same. This will make it easier to batch process the images. Since the optical probes are small and easy to handle, the possibility of placing

the probes all around the object was explored. A schematic of the suggested experimental setup is shown in figure 61.

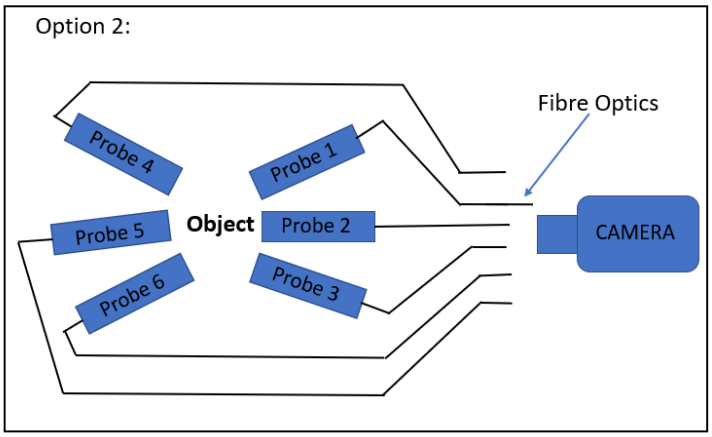

Figure 61. Suggested experimental setup with probes placed on either side of the object.

Since 6 probes were not available, the experiment was carried out by placing the pin on a rotary post and imaging it at various angles using a single probe and camera. Figure 62. shows the reconstruction obtained using the following angles: 0°/35°/150°/165°/210°/330°. The quality was not as good as the one obtained using 6 front angles. This was attributed to the fact that 150° and 330° are exactly opposite to each other, thus not following the conditions of non-collinearity. Also, imaging with 35° and 210° is equivalent to imaging at 30° and 35°, which might be too close, leading to elongation of the sphere. Thus, it can be concluded that the use of back angles might be redundant unless the angles are chosen such that they have a good separation.

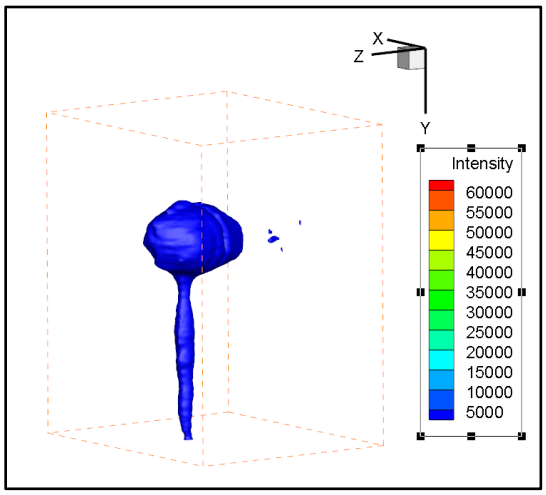

Figure 62. 3D image for reconstruction with front and back angles.

3.3.2 Reconstructions using Probe and Imaging Fiber

In order to use one camera for imaging, optical fibers need to be used to transmit the image plane data from different viewing angles to the camera. Thus, the reconstruction of the pin using the probe and optical fiber assembly was carried out. The images were obtained using a single probe and imaging fiber by rotating the object through required angles.

Since the resolution of the system with the fiber was seen to reduce (section (2.4)) the obtained images suffered from the diffraction of light. Figure 63 shows the spreading of light around the sphere. Since the reconstructions are dependent on the light intensity, the quality of the reconstructions was seen to reduce significantly.

The average standard deviation for the reconstruction of the calibration plate was much higher for the images with probe and fiber optic assembly. It has been discussed by Sacarano [28] that 'the first indication of good quality reconstruction is the residual of the curve fitting method used during calibration'. A value greater than 0.5 pixels represents that the curve fitting method used is not good enough for obtaining good quality reconstructions. As shown in Table 12, the value for the probe and imaging fiber assembly is greater than 1, thus indicating the need for better calibration models or pre-processing for the images.

The sliced view in figure 64 shows a lot of noise around the boundaries of the sphere which indicates the spreading of light. Also, the loss of contrast near the stem makes it very difficult to distinguish it from the background. The spreading of light especially has an adverse effect on the geometry of the figure causing the sphere to be elongated at the crown (Refer to Figure 64). However, the dimensions of the obtained figure were similar to the original pin dimensions.

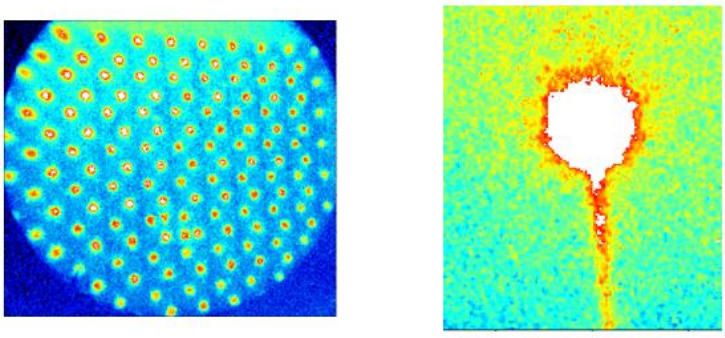

Figure 63. Raw images of the test target (left); and object(right) using probe and fiber optic assembly.

Table 12. Average standard deviation for reconstruction of the calibration plate.

	Average Standard Deviation in pixels (6 angles)
Probe	0.4464
Probe + Fiber Optic	1.325

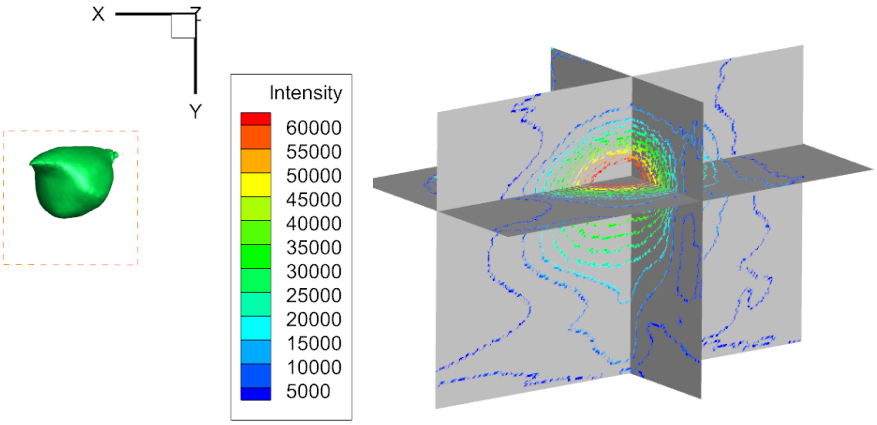

Figure 64. 3D Reconstruction with 6 viewing angles (0-15-30-40-345-330) (left); sliced view of reconstruction (right).

3.4 Conclusion

Increasing the number of viewing angles improves the reconstruction quality up to a certain limit (6 or 7 angles). Increasing the number of angles beyond 7 increases the standard deviation of calibration and will not lead to significantly better results. Similarly, more than 30 iterations will not make any difference to the reconstruction accuracy.

Fiber optics work on the principle of total internal reflections. The light rays will reflect back at the surface of each fiber due to the high refractive index of the core. Since this process is not perfect, some amount of light will be refracted. This can be seen in the form of the spreading of light around the boundaries of the sphere. Using a fiber bundle with more fibers can improve the accuracy of light travel thus improving the reconstruction quality.

Thus, it can be concluded that using the probe and fiber optic arrangement for Tomographic PIV measurements or 3D reconstruction experiments is possible but with certain improvements to the experimental setup.

Since a sufficient number of fibers were not available an experimental setup with two probes and fibers was installed in order to determine any shortcomings or limitations of the setup. Following observations were made:

- Figure 65 shows the experimental setup with two probes and optical fibers. Since the image conduit is non-flexible it was positioned at a viewing angle of 0°. The flexible imagining fiber was placed at a viewing angle of 150°. As explained in section (2.3.1), the best resolution was obtained using the point grey chameleon 2.0 camera with a long microscopic lens. The camera has a maximum resolution of 1296(H)X964(V) with a pixel size of 3.75µmX3.75µm. The optical fiber has an image circle diameter of 1.85mm (average value) and a coating diameter of 2.4mm. The image conduit has an outer diameter of 3.2mm. Thus, even when the image conduit and fiber optic are placed touching each other their dimensions are bigger than the camera chip size. Also, the PointGrey camera can be operated at a maximum of 18fps. The frame rate might be insufficient for imaging flows or explosive materials. Thus, a camera with a bigger chip size and higher image capturing speed should be used.

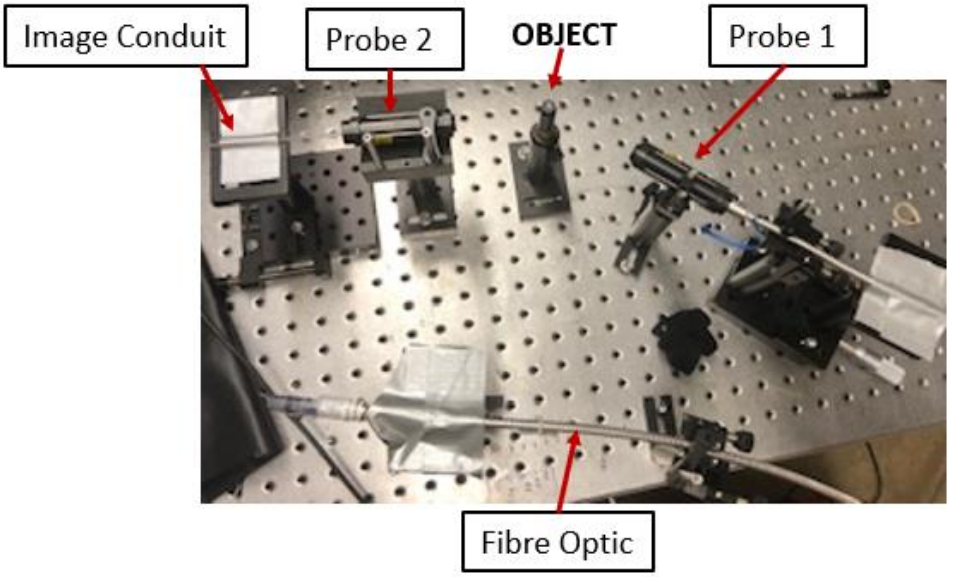

Figure 65. Experimental Setup with two probes and imaging fibers.

- FastCam SA-Z was used to image a propane open torch flame using the two-probe setup. FastCam SA-Z has a frame speed of 20,000fps at a resolution of 1024 X 1024 pixels. The pixel dimensions are 20µm X 20µm. The size of the sensor is thus, 20.48mm X 20.48mm. Since the fiber diameters are of the order of 2.4 mm, the obtained images are very small and need to be magnified in order to use them for further analysis (Figure 66). As suggested in section 3.3.1, optimum results will be obtained when 6 viewing angles are used. Thus, considering 6 fiber heads are placed at the imaging plane in two rows of three fibers each, then the fibers will occupy a minimum area of 360 X 240 pixels, considering the fibers to be touching each other. However, in practice, the fibers will be placed slightly further away

and a resolution of 640 X 280 pixels might be sufficient to obtain good results. The required resolution can be obtained when the camera is operated at 100,000 fps.

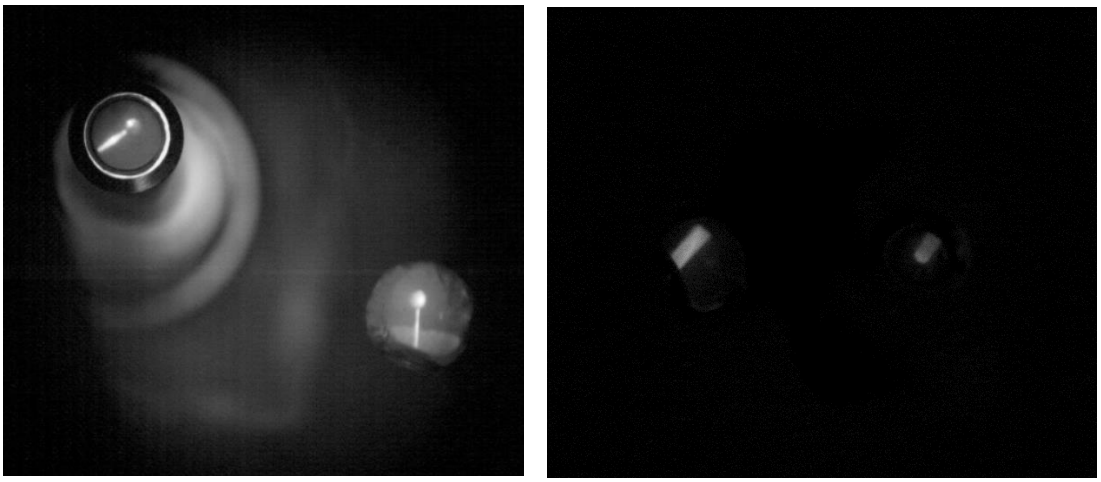

Figure 66. Image of pin (left); and propane air torch (right) using two probes.

4. SUMMARY AND FUTURE WORK

From the discussions above it can be concluded that the probe and fiber optic assembly will be suitable for engine diagnostics as well as for Tomo-PIV experiments

A 3D printed probe was fitted onto the engine cylinder to verify the design. The probe fits perfectly in the pressure transducer hole. However, the manufacturing of the entire probe will be costly and time-consuming due to the small size of the parts needed to build the entire probe. Since the problem of soot deposition has not been considered in the design, the probe might have to be removed after a couple of runs so as to clear the sapphire window. The design of the cap can be modified as per the design of the self-cleaning probe mentioned by Yan et al. [14]. Since the lens design does not occupy the entire pressure transducer length, rod lenses can be used instead of the spherical lenses so as to improve the resolution and minimize losses. The two-color method for temperature detection can be easily implemented using this probe design for preliminary diagnostics.

Similarly, for PIV applications, the use of fiber optics with a higher number of fibers should be explored. If a high-speed camera is used with a higher frame rate the experimental setup design suggested in section 3.3.1 can be easily implemented. Another option to improve the magnification is the use of two camera lenses, one with high focal length and the other with a low focal length. The lenses are placed in front of each other so that a high magnification can be achieved. The optical probe can be completely built using commercially available materials with good repeatability at a reasonable cost. Thus, the probe design can prove to be a very good alternative for explosive testing environments so as to avoid any damages to the camera.

REFERENCES

[1]. Shakal, J. S., & Martin, J. K. (1994). Imaging and Spatially Resolved Two-Color Temperature Measurements Through a Coherent Fiberoptic: Observation of Auxiliary Fuel Injection Effects on Combustion in a Two-Stroke DI Diesel. *SAE transactions*. 1441-1453.

[2]. Bowditch, F. W. (1961). A new tool for combustion research a quartz piston engine (No. 610002). *SAE Technical Paper*.

[3]. Zhao, H., Lowry, G., & Ladommatos, N. (1996). Time-resolved measurements and analysis of in-cylinder gases and particulates in compression-ignition engines. *SAE transactions*, 1542-1560.

[4]. Mark Linne (2016). Advanced Laser Diagnostics for Combustion Research. Retrieved from https://cefrc.princeton.edu/sites/cefrc/files/combustion-summer-school/lecture-notes/Advanced-Laser-Diagnostics-in-Combustion-Research_Linne.pdf

[5]. Baker, H. D. and Ryder, E. A. (1961), Temperature Measurement in Engineering, Vol. 2. John Wiley &d Sons

[6]. Zhao, H., & Ladommatos, N. (1998). Optical diagnostics for soot and temperature measurement in diesel engines. *Progress in energy and combustion science*, *24*(3), 221-255

[7]. O. A. Uyehara, P. S. Myers, K. M. Watson, and L. A. Wilson (1946), "Flame Temperature Measurements in Internal Combustion Engines." *ASME Trans*., Vol. 68, pp. 17- 30

[8]. Heywood, J. B. (1988). Internal combustion engine fundamentals, pp. 668-682

[9]. Payri, F., Pastor, J. V., García, J. M., & Pastor, J. M. (2007). Contribution to the application of two-color imaging to diesel combustion. *Measurement science and technology*, *18*(8), 2579.

[10]. Arcoumanis, C., Bae, C., Nagwaney, A., & Whitelaw, J. H. (1995). Effect of EGR on combustion development in a 1.9 L DI diesel optical engine. *SAE transactions*, 1491-1515.

[11]. Zhao, H. (2012). Laser diagnostics and optical measurement techniques in internal combustion engines. *SAE*. pp.130 -160

[12]. Johansen, L. C. R., & Hemdal, S. (2015). In-cylinder visualization of stratified combustion of E85 and main sources of soot formation. *Fuel*, *159*, 392-411.

[13]. Dierksheide, U., Meyer, P., Hovestadt, T., & Hentschel, W. (2002). Endoscopic 2D particle image velocimetry (PIV) flow field measurements in IC engines. *Experiments in fluids*, *33*(6), 794-800.

[14]. Yan, J., & Borman, G. L. (1988). Analysis and in-cylinder measurement of particulate radiant emissions and temperature in a direct injection diesel engine. *SAE transactions*, 1623-1644.

[15]. Matsui, Y., Kamimoto, T., & Matsuoka, S. (1980). A study on the application of the two–color method to the measurement of flame temperature and soot concentration in diesel engines. *SAE Transactions*, 3043-3055.

[16]. Witze, P. O., Hall, M. J., & Wallace, J. S. (1988). Fiber-optic instrumented spark plug for measuring early flame development in spark ignition engines (No. 881638). *SAE Technical Paper*.

[17]. Kranz, P., Fuhrmann, D., Goschütz, M., Kaiser, S., Bauke, S., Golibrzuch, K., & Zachow, J. (2018). In-Cylinder LIF Imaging, IR-Absorption Point Measurements, and a CFD Simulation to Evaluate Mixture Formation in a CNG-Fueled Engine. *SAE International Journal of Engines*, *11*(2018-01-0633), 1221-1238.

[18]. Hall, M. J., & Koenig, M. (1996, January). A fiber-optic probe to measure precombustion in-cylinder fuel-air ratio fluctuations in production engines. In Symposium (International) on Combustion (Vol. 26, No. 2, pp. 2613-2618). *Elsevier*.

[19]. Meyer, T. R., & White, R. A. (1998). The effects of cylinder head deformation and asymmetry on exhaust valve thermo-mechanical stresses. *SAE transactions*, 1515-1523.

[20]. Diviš, M., Tichánek, R., & Španiel, M. (2003). Heat transfer analysis of a diesel engine head. *Acta Polytechnica*, 43(5).

[21]. Smith, Warren J. "Chapter 15.8 The Modulation Transfer Function." In *Modern Optical Engineering*, 385-90. 4th ed. New York, NY: McGraw-Hill Education, 2008.

[22]. John G. Savard (2001). The Five Seidel Aberrations. Retrieved from http://www.quadibloc.com/science/opt0505.htm

[23]. Dereniak, Eustace L., and Teresa D. Dereniak, (2008), Geometrical and Trigonometric Optics, Cambridge University Press

[24]. Lakhtakia, A., & Martín-Palma, R. J. (Eds.). (2013). *Engineered biomimicry*. Newnes.pp 1-36

[25]. Raffel, M., Willert, C. E., Scarano, F., Kähler, C. J., Wereley, S. T., & Kompenhans, J. (2018). Particle image velocimetry: a practical guide. *Springer*, pp 1-29, 309-335

[26]. Elsinga, G. E., Scarano, F., Wieneke, B., & van Oudheusden, B. W. (2006). Tomographic particle image velocimetry. *Experiments in fluids*, *41*(6), 933-947.

[27]. Scarano, F., & Poelma, C. (2009). Three-dimensional vorticity patterns of cylinder wakes. *Experiments in Fluids*, *47*(1), 69.

[28]. Scarano, F. (2012). Tomographic PIV: principles and practice. *Measurement Science and Technology*, *24*(1), 012001.

[29]. Lynch, K. P., & Scarano, F. (2015). An efficient and accurate approach to MTE-MART for time-resolved tomographic PIV. *Experiments in Fluids*, *56*(3), 66.

[30]. Thomas, L., Tremblais, B., & David, L. (2014). Optimization of the volume reconstruction for classical Tomo-PIV algorithms (MART, BIMART and SMART): synthetic and experimental studies. *Measurement Science and Technology*, *25*(3), 035303.

[31]. Ghaemi, S., & Scarano, F. (2010). Multi-pass light amplification for tomographic particle image velocimetry applications. *Measurement science and technology*, *21*(12), 127002.

[32]. FlowMaster Tomographic PIV. Retrieved from https://www.lavision.de/en/products/flowmaster/tomographic-piv/

[33]. Edmund Optics. Distortion. Retrieved from https://www.edmundoptics.com/resources/application-notes/imaging/distortion/

[34]. Li, G., & Wang, P. (2013). Advanced analysis and design for fire safety of steel structures. Pp 37-65. *Springer Science & Business Media*.

[35]. Jiang, N., Bao, Q., & Yang, S. (2015). 3D Reconstruction technique for tomographic PIV. *Transactions of Tianjin University*, *21*(6), 533-540.

[36]. Knight Optical (17 December 2018). The Benefits and Uses of Sapphire Optical Windows. Retrieved from https://www.knightoptical.com/about-us/news/the-benefits-and-uses-of-sapphire-optical-windows/

[37]. Meyer, T. R., Brear, M., Jin, S. H., & Gord, J. R. (2010). Formation and diagnostics of sprays in combustion. *Handbook of Combustion: Online*, 291-322.

[38]. Halls, B. R., Thul, D. J., Michaelis, D., Roy, S., Meyer, T. R., & Gord, J. R. (2016). Single-shot, volumetrically illuminated, three-dimensional, tomographic laser-induced-fluorescence imaging in a gaseous free jet. *Optics express*, *24*(9), 10040-10049.

[39]. Meyer, T. R., Halls, B. R., Jiang, N., Slipchenko, M. N., Roy, S., & Gord, J. R. (2016). High-speed, three-dimensional tomographic laser-induced incandescence imaging of soot volume fraction in turbulent flames. *Optics express*, *24*(26), 29547-29555.

[40]. Halls, B. R., Thul, D. J., Michaelis, D., Roy, S., Meyer, T. R., & Gord, J. R. (2016). Single-shot, volumetrically illuminated, three-dimensional, tomographic laser-induced-fluorescence imaging in a gaseous free jet. *Optics express*, *24*(9), 10040-10049.

[41]. Halls, B. R., Hsu, P. S., Jiang, N., Legge, E. S., Felver, J. J., Slipchenko, M. N., ... & Gord, J. R. (2017). kHz-rate four-dimensional fluorescence tomography using an ultraviolet-tunable narrowband burst-mode optical parametric oscillator. *Optica*, *4*(8), 897-902.